

000 001 002 003 004 005 006 007 008 009 010 011 012 013 014 015 016 017 018 019 020 021 022 023 024 025 026 027 028 029 030 031 032 033 034 035 036 037 038 039 040 041 042 043 044 045 046 047 048 049 050 051 052 053 SAFEFLOWMATCHER: SAFE AND FAST PLANNING USING FLOW MATCHING WITH CONTROL BARRIER FUNCTIONS

Anonymous authors

Paper under double-blind review

ABSTRACT

Generative planners based on flow matching (FM) produce high-quality paths in a single or a few ODE steps, but their sampling dynamics offer no formal safety guarantees and can yield incomplete paths near constraints. We present *SafeFlowMatcher*, a planning framework that couples FM with control barrier functions (CBFs) to achieve *both* real-time efficiency and certified safety. SafeFlowMatcher uses a two-phase *prediction–correction* (PC) integrator: (i) a prediction phase integrates the learned FM once (or a few steps) to obtain a candidate path without intervention; (ii) a correction phase refines this path with a vanishing time-scaled vector field and a CBF-based quadratic program that minimally perturbs the vector field. We prove a barrier certificate for the resulting flow system, establishing forward invariance of a robust safe set and finite-time convergence to the safe set. In addition, by enforcing safety only on the executed path—rather than all intermediate latent paths—SafeFlowMatcher avoids distributional drift and mitigates local trap problems. Moreover, SafeFlowMatcher attains faster, smoother, and safer paths than diffusion- and FM-based baselines on maze navigation, locomotion, and robot manipulation tasks. Extensive ablations corroborate the contributions of the PC integrator and the barrier certificate.

1 INTRODUCTION

Robotic path planning must simultaneously achieve real-time responsiveness and strong safety guarantees. Recently, generative models such as diffusion (Ho et al., 2020; Dhariwal & Nichol, 2021; Song et al., 2021b) and flow matching (FM) (Lipman et al., 2023) have gained attention for path planning, thanks to their expressive modeling of multi-modal action distributions (Carvalho et al., 2023; Braun et al., 2024) and low-latency inference (Qureshi et al., 2019; Liu et al., 2024) compared to classical sampling- and optimization-based planners. However, the sampling dynamics of these models are governed by implicitly learned rules and can produce paths that violate physical safety constraints, leading to task interruptions or collisions. Therefore, integrating *certified safety* into generative planning is essential for deployment in real-world robotic systems.

Several approaches have attempted to enforce safety in generative planning. Safety-guidance methods regulate the sampling process through learned safety scores (often called guidance, e.g., classifier-free guidance (Dhariwal & Nichol, 2021; Ho & Salimans, 2021), or value/reward guidance (Yang et al., 2024; Chen et al., 2024)), but their reliance on data-driven proxy prevents them

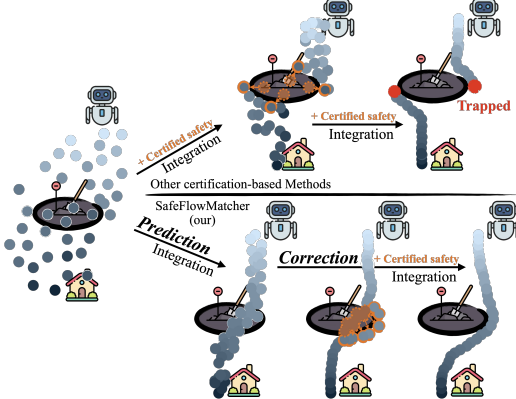


Figure 1: **Overview of SafeFlowMatcher Versus Existing Certification-Based Methods.** Directly constraining intermediate samples during generation (top) can cause paths to be distorted or trapped, whereas SafeFlowMatcher (bottom) decouples generation and certification, producing a complete and certified-safe path.

from providing strong safety guarantees. More explicitly, certification-based methods incorporate functions such as Control Barrier Functions (CBFs) directly into the generative process (Xiao et al., 2025). Unlike guidance-based approaches, these methods can guarantee safety at deployment without requiring additional training. However, a key challenge in such certification-based methods is a *semantic misalignment*: certification concerns the executed physical path (its waypoints over the horizon), whereas interventions are often applied to intermediate latent states that are never executed. Constraining such latents is unnecessary for certification. As a result, repeated interventions distort the learned flow and often yield incomplete (locally trapped) paths. Finally, although diffusion samplers can be accelerated (Lu et al., 2022; Zhang & Chen, 2022; Liu et al., 2022), their SDE-based denoising requires many steps, making real-time planning expensive. In contrast, FM casts sampling as deterministic ODE integration, generating accurate paths in a *single* or a *few* steps.

To address these limitations, we propose *SafeFlowMatcher*, a planning framework that combines flow matching with CBFs, particularly for finite-time convergence CBFs, to achieve certified safety before the completion of generation, while maintaining the efficiency of FM. Our key idea is a *prediction–correction* (PC) integrator that decouples distributional drift from safety certification. In the prediction phase, we propagate the flow once (or a few steps) to obtain a candidate path without any safety intervention. In the correction phase, we refine this path by (i) compensating for integration error through a modified vector field, and (ii) enforcing safety through CBFs. Rather than constraining all intermediate samples from pure noise to the target during prediction, SafeFlowMatcher enforces safety only in the correction phase. This preserves the native FM dynamics and prevents distributional drift when generating the target path. Also, it avoids local traps caused by repeatedly pushing intermediate waypoints onto the barrier boundary and stalling near safety constraints.

Our main contributions are as follows:

- We introduce SafeFlowMatcher, a novel planning framework that integrates finite-time convergence CBF-based certification with flow matching to enforce hard safety constraints, while preserving the efficiency of flow matching.
- We propose prediction–correction integrator that decouples path generation from certification: FM first generates paths without intervention, and then CBF-based corrections enforce finite-time convergence to the safe set while compensating for integration errors.
- We validate SafeFlowMatcher in maze navigation, locomotion, and robot manipulation tasks with extensive ablation studies, showing consistent improvements over both FM- and diffusion-based planners in efficiency, safety, and path quality.

2 RELATED WORK & PRELIMINARIES

2.1 FLOWMATCHER: FLOW MATCHING FOR PLANNING

FM has recently been proposed as a powerful alternative to diffusion, originally in the image generation domain (Lipman et al., 2023; Song et al., 2021b), and has shown promise for efficient path planning and robotic control (Ye & Gombolay, 2024; Zhang & Gienger, 2024; Chisari et al., 2024; Xing et al., 2025). Unlike diffusion, FM directly learns a time-varying vector field that maps noise to the target distribution via forward integration, making the sampling process efficient and flexible.

We adapt standard flow matching (FM) (Lipman et al., 2023) to the planning context. Let $H \in \mathbb{N}$ be the planning horizon and $\mathcal{H} \triangleq \{0, \dots, H\}$. A path is a stacked vector $\boldsymbol{\tau} = (\boldsymbol{\tau}^0, \boldsymbol{\tau}^1, \dots, \boldsymbol{\tau}^H) \in \mathcal{D}^{H+1} \subseteq \mathbb{R}^{d \times (H+1)}$, where each waypoint $\boldsymbol{\tau}^k \in \mathcal{D} \subseteq \mathbb{R}^d$ encodes the state at step k .

Let $v_t(\cdot; \theta) : \mathcal{D}^{H+1} \rightarrow \mathcal{D}^{H+1}$ be a time-dependent vector field. The flow $\psi : [0, 1] \times \mathcal{D}^{H+1} \rightarrow \mathcal{D}^{H+1}$ is defined as the solution of the ODE

$$\frac{d}{dt} \psi_t(\boldsymbol{\tau}) = v_t(\psi_t(\boldsymbol{\tau}); \theta), \quad \psi_0(\boldsymbol{\tau}) = \boldsymbol{\tau}, \quad (1)$$

which transports a simple prior p_0 (e.g. $\mathcal{N}(0, I)$) to a target p_1 . Following conditional flow matching (CFM), we train $v_t(\cdot; \theta)$ by regressing it to a conditional vector field that generates a fixed conditional probability path. We adopt the optimal transport (OT) path $p_t(\boldsymbol{\tau} \mid \boldsymbol{\tau}_1) = \mathcal{N}(\boldsymbol{\tau}; \mu_t(\boldsymbol{\tau}_1), \sigma_t^2 I)$, $\mu_t(\boldsymbol{\tau}_1) = t \boldsymbol{\tau}_1$, $\sigma_t = 1 - t$, whose generating *OT-conditional vector field* is

$$u_t(\boldsymbol{\tau} \mid \boldsymbol{\tau}_1) = \frac{\boldsymbol{\tau}_1 - \boldsymbol{\tau}}{1 - t}. \quad (2)$$

108 Let q denote the data distribution over the target paths τ_1 . Sampling $t \sim \text{Unif}[0, 1]$, $\tau_0 \sim p_0$, $\tau_1 \sim q$
 109 and defining $\tau_t \triangleq \psi_t(\tau_0) = (1-t)\tau_0 + t\tau_1$ (conditioned on τ_1), we have by (2) that $u_t(\tau_t \mid \tau_1) =$
 110 $\tau_1 - \tau_0$. Hence, we train $v_t(\cdot; \theta)$ with the CFM loss:

$$111 \quad \mathcal{L}(\theta) = \mathbb{E}_{t, q(\tau_1), p_0(\tau_0)} \|v_t(\psi(\tau_0); \theta) - (\tau_1 - \tau_0)\|_2^2. \quad (3)$$

112 Further details are in Lipman et al. (2023).

113 For numerical integration, we discretize $0 = t_0 < \dots < t_T = 1$ with the sampling horizon $T \in \mathbb{N}$
 114 (Collectively $\mathcal{T}(T) = \{t_0, \dots, t_T\}$) and define step sizes $\Delta t_i = t_{i+1} - t_i$. We define T -step in-
 115 tegrator $\Psi_{0 \rightarrow 1}^{(T)} : \mathcal{D}^{H+1} \rightarrow \mathcal{D}^{H+1}$ (e.g., Euler integrator ¹) which integrates the flow matching
 116 dynamics from τ_0 to τ_1 as

$$117 \quad \Psi_{0 \rightarrow 1}^{(T)}(\tau_0) = \tau_0 + \sum_{i=0}^{T-1} \Delta t_i v_{t_i}(\tau_{t_i}; \theta). \quad (4)$$

122 CONTROL BARRIER FUNCTIONS

123 *Safety filters* (Hsu et al., 2023; Wabersich et al., 2023) are a real-time intervention mechanism to
 124 ensure that an autonomous agent operates within some predefined safety sets, overriding its nominal
 125 behavior only when it is about to violate the sets. Various approaches exist for constructing safety
 126 filters, but among these, *control barrier functions* (CBFs) (Ames et al., 2019) are especially popular,
 127 as they provide a systematic way to guarantee forward invariance of safe sets by solving a real-time
 128 optimization problem at each control step. Additional recent work on CBFs, including non-convex
 129 safe sets and learning-based CBFs, are summarized in Appendix A.

130 Here, we review only the standard finite-time convergence CBF preliminaries that are necessary for
 131 the rest of this paper. To this end, we consider an arbitrary control-affine system

$$133 \quad \dot{\mathbf{x}}_t = f(\mathbf{x}_t) + g(\mathbf{x}_t)\mathbf{u}_t, \quad (5)$$

134 where $\mathbf{x}_t \in \mathcal{D} \subset \mathbb{R}^d$, $\mathbf{u}_t \in \mathcal{U} \subset \mathbb{R}^d$, and $f : \mathbb{R}^d \rightarrow \mathbb{R}^d$ and $g : \mathbb{R}^d \rightarrow \mathbb{R}^{d \times d}$ are locally Lipschitz
 135 continuous.

136 Define the *safe set* \mathcal{C} as the superlevel set of a continuously-differentiable (C^1) function $b : \mathcal{D} \rightarrow \mathbb{R}$,

$$137 \quad \mathcal{C} \triangleq \{\mathbf{x}_t \in \mathcal{D} \mid b(\mathbf{x}_t) \geq 0\}. \quad (6)$$

138 System safety is often mathematically prescribed by ensuring that a system's state safely converges
 139 to the targeted safe set within finite time.

140 **Definition 1 (Finite-Time Convergence CBF)** *Given the system (5) and the safe set (6), C^1 func-
 141 tion b is called a finite-time convergence CBF if there exist parameters $\rho \in [0, 1)$ and $\epsilon > 0$ such
 142 that for all $\mathbf{x}_t \in \mathcal{D}$,*

$$143 \quad \sup_{\mathbf{u}_t \in \mathcal{U}} [L_f b(\mathbf{x}_t) + L_g b(\mathbf{x}_t)\mathbf{u}_t + \epsilon \cdot \text{sgn}(b(\mathbf{x}_t))|b(\mathbf{x}_t)|^\rho] \geq 0, \quad (7)$$

144 where $L_f b(\mathbf{x}_t) \triangleq \nabla b(\mathbf{x}_t)^\top f(\mathbf{x}_t)$ and $L_g b(\mathbf{x}_t) \triangleq \nabla b(\mathbf{x}_t)^\top g(\mathbf{x}_t)$ denote the Lie derivatives of b along
 145 f and g , respectively.

146 **Lemma 1 (Forward Invariance of the Safe Set)** *Define CBF b as in Definition 1, such that the
 147 initial state satisfies $b(\mathbf{x}_0) \geq 0$. Any Lipschitz continuous controller \mathbf{u}_t that satisfies condition (7)
 148 ensures forward invariance of the safe set \mathcal{C} , i.e., $b(\mathbf{x}_t) \geq 0$ for all $t \geq 0$.*

149 Lemma 1 ensures that once the state first enters the safe set, it remains there thereafter. To select a
 150 control input that guarantees forward invariance of \mathcal{C} as well as become close as possible to some
 151 reference control input $\mathbf{u}_t^{\text{ref}}$, a common approach is to solve a quadratic program (CBF-QP) (Ames
 152 et al., 2019) at each time step:

$$153 \quad \mathbf{u}_t^* = \arg \min_{\mathbf{u}_t \in \mathcal{U}} \|\mathbf{u}_t - \mathbf{u}_t^{\text{ref}}\|^2 \quad \text{subject to} \quad L_f b(\mathbf{x}_t) + L_g b(\mathbf{x}_t)\mathbf{u}_t + \epsilon \cdot \text{sgn}(b(\mathbf{x}_t))|b(\mathbf{x}_t)|^\rho \geq 0. \quad (8)$$

154 This means the optimal solution \mathbf{u}_t^* is the minimally modified control that guarantees the forward
 155 invariance of the safe set \mathcal{C} . Moreover, based on the finite-time stability theorem (Bhat & Bernstein,
 156 2000), the finite-time convergence CBF can be used to ensure that states not only remain within the
 157 safe set but also reach it within finite-time (Li et al., 2018; Srinivasan et al., 2018).

158 ¹Alternatively, higher-order ODE solvers can be used.

162

3 SAFEFLOWMATCHER

164 Here, we present *SafeFlowMatcher*, a safe and fast planning framework that couples flow matching
 165 with certified safety in settings where neither the dynamics nor cost map are known. First, in Sec-
 166 tion 3.1, we introduce a two-phase *prediction–correction* (PC) integrator which decouples genera-
 167 tion and certification. Next, in Section 3.2, we formalize safety for SafeFlowMatcher by employing
 168 control barrier functions (CBFs) and derive conditions that guarantee forward invariance and finite-
 169 time convergence to the safe set. The pseudocode of SafeFlowMatcher is in Algorithm 1, and full
 170 generation processes for two Maze environments are visualized in Appendix F.5.

171 We introduce a crucial problem in non-autoregressive planner, par-
 172 ticularly for a generative-based planner. As shown in Figure 2, non-
 173 autoregressive planners may fail to generate a complete path after
 174 planning when using CBFs. Although the resulting path remains
 175 safe (does not exceed safety constraints), it may be unable to reach
 176 the goal because certain waypoints become *locally trapped* near the
 177 barrier boundaries and cannot escape within the finite sampling or
 178 integration time. We will show that SafeFlowMatcher can effec-
 179 tively resolve this issue using a PC integrator.

180 **Definition 2 (Local Trap)** A local trap problem occurs during the
 181 planning process if there exists $k \in \mathcal{H}$ such that $\|\tau_1^k - \tau_1^{k-1}\| > \zeta$,
 182 where $\zeta > 0$ is a user-defined threshold depending on the planning
 183 environment.²

185 **Algorithm 1** SafeFlowMatcher

187 **Input:** learned velocity field $v_t(\cdot; \theta)$, prediction and correction horizon T^p, T^c , planning horizon
 188 \mathcal{H} , CBF parameters (ϵ, ρ) , robustness parameter δ , and scale constant α
 189 **Output:** Safe path τ_1^c

190 **Phase 1: Prediction**

191 1: Sample initial noise $\tau_0^p \sim \mathcal{N}(0, I)$
 192 2: Compute predicted path $\tau_1^p \leftarrow \Psi_{0 \rightarrow 1}^{(T^p)}(\tau_0^p)$ by (9)

193 **Phase 2: Correction**

194 3: Initialize corrected path $\tau_0^c \leftarrow \tau_1^p$
 195 4: **for** each correction step $t \in \mathcal{T}(T^c)$ **do**
 196 5: $\tilde{v}_t \leftarrow \alpha(1-t)v_t(\tau_t^c; \theta)$
 197 6: **for** each waypoint $k \in \mathcal{H}$ **do**
 198 7: Solve QP (17) to obtain $(\mathbf{u}_t^{k*}, r_t^{k*})$, using \tilde{v}_t
 199 8: **end for**
 200 9: Update velocity time-scaled flow dynamics (13) with $\mathbf{u}_t^* = \{\mathbf{u}_t^{0,*}, \dots, \mathbf{u}_t^{H,*}\}$
 201 10: **end for**
 202 11: Return safe final path τ_1^c

204

3.1 PREDICTION–CORRECTION INTEGRATOR

205 SafeFlowMatcher divides the integration process into two phases: a prediction phase that generates
 206 an approximate path without considering safety, and a correction phase that refines the path by
 207 reducing integration error and adding safety constraints. Let $\tau_t^\ell \in \mathcal{D}^{H+1} \subseteq \mathbb{R}^{d \times (H+1)}$ for $\ell \in \{p, c\}$
 208 denote the paths in the prediction and correction phases, with waypoints $\tau_t^{\ell,k} \in \mathcal{D} \subseteq \mathbb{R}^d$ for $k \in \mathcal{H}$.
 209 Additionally, we denote by $T = T^p + T^c$ the total sampling horizon, where T^p and T^c are the number
 210 of sampling (integration) steps allocated to the prediction and correction phases, respectively.

212 The **Prediction phase** aims to quickly approximate the target path starting from pure noise $\tau_0^p \sim$
 213 $\mathcal{N}(0, I)$, without considering safety constraints. Starting from the noise, we run Euler integration to

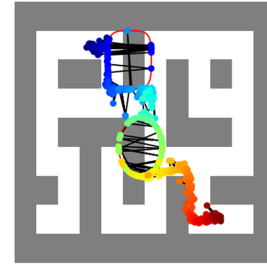


Figure 2: **Local trap.** Example of a local trap in maze environment.

²The definition is slightly different from that of SafeDiffuser (Xiao et al., 2025) to capture a broader class of failure cases. See Appendix D for the details.

216 obtain the solution of the flow matching dynamics (1):
 217

$$\tau_1^p = \Psi_{0 \rightarrow 1}^{(T^p)}(\tau_0^p) = \tau_1^* + \varepsilon, \quad (9)$$

219 where τ_1^* is the exact solution of the flow matching dynamics and ε is the Euler integration (pre-
 220 prediction) error. To balance computational efficiency and reliability, we select small T^p (typically
 221 $T^p = 1$) that places τ_1^p sufficiently close to τ_1^* , making it a suitable initialization for the correction
 222 phase.

223 The **Correction phase** starts from the path in the prediction phase $\tau_0^c = \tau_1^p$, unlike τ_0^p in the
 224 prediction phase. In this phase, the path is refined by (i) reducing the discretization error ε and (ii)
 225 enforcing safety constraints.
 226

227 To achieve (i), we introduce the *vanishing time-scaled flow dynamics* (VTFD)
 228

$$\frac{d\tau_t^c}{dt} = \alpha(1-t)v_t(\tau_t^c; \theta) \triangleq \tilde{v}_t(\tau_t^c; \theta), \quad (10)$$

230 where the factor $(1-t)$ gradually suppresses the vector field as $t \rightarrow 1$ with scaling constant $\alpha > 0$.
 231 Intuitively, this produces a contraction effect: the path is driven toward the target direction in the
 232 early correction steps, while the dynamics become increasingly stable near $t=1$, preventing drift
 233 and allowing the prediction error to decay. This mechanism is formalized in Lemma 2 and Lemma 3.
 234

235 **Lemma 2** *Assume the prediction error $\varepsilon \sim p_\varepsilon$ has a symmetric, zero-mean distribution (e.g., Gaussian)
 236 and that, in a neighborhood of $\varepsilon = 0$, the negative log-density $-\log p_\varepsilon$ is C^2 with a positive-
 237 definite Hessian $A \succ 0$ (i.e., locally strongly convex). In addition, assume the target log-density
 238 $\log p_1$ is C^2 . Suppose the correction phase is initialized near the target τ_1^* :*

$$\tau_t^c = \tau_1^* + (1-t)\varepsilon, \quad \varepsilon = O(1). \quad (11)$$

239 Then, $\mathbb{E}[\tau_1 | \tau_t^c] = \tau_1^* + O(1-t)$.
 240

241 We empirically verify the validity of the symmetric zero-mean assumption on the prediction error ε
 242 in Appendix B.1. (11) is a natural result under optimal transport, since OT path approaches τ_1 as
 243 $t \rightarrow 1$. Lemma 2 ensures that the posterior expectation contracts toward the target.
 244

245 **Lemma 3** *Under the assumptions of Lemma 2, let $\mathbf{e}_t \triangleq \tau_t^c - \tau_1^*$. If the flow dynamics follow the
 246 vanishing time-scaled flow dynamics (10), then as $t \rightarrow 1$,*

$$\mathbf{e}_t = O((1-t)^2) + (\varepsilon + O(1))e^{-\alpha t}. \quad (12)$$

247 Lemma 3 implies that VTFD reduces the prediction error of τ_1^c . See the proofs of Lemma 2 and
 248 Lemma 3 in Appendix B.2.
 249

250 3.2 CONTROL BARRIER CERTIFICATE FOR SAFEFLOWMATCHER

251 To ensure the safety constraints hold during the correction phase, we introduce an additional pertur-
 252 bation to minimally intervene the flow dynamics (10):
 253

$$\frac{d\tau_t^c}{dt} = \tilde{v}_t(\tau_t^c; \theta) + \Delta \mathbf{u}_t, \quad (13)$$

254 where \tilde{v}_t is VTFD defined in (10), and $\Delta \mathbf{u}_t = \{\Delta \mathbf{u}_t^0, \Delta \mathbf{u}_t^1, \dots, \Delta \mathbf{u}_t^H\} \in \mathbb{R}^{d \times (H+1)}$ ($\Delta \mathbf{u}_t^k \in \mathbb{R}^d$) is a
 255 perturbation term that enforces safety constraints. Importantly, the safety constraint is applied in a
 256 *waypoint-wise* fashion: the CBF condition is enforced independently for each waypoint $\tau_t^{c,k}$ so that
 257 it remains within safe set \mathcal{C} . Thus, we can split the dynamics (13) into
 258

$$\frac{d\tau_t^{c,k}}{dt} = \tilde{v}_t^k(\tau_t^c; \theta) + \Delta \mathbf{u}_t^k \triangleq \mathbf{u}_t^k, \quad (14)$$

259 where $\tilde{v}_t^k(\tau_t^c; \theta)$ denotes the k -th column of $\tilde{v}_t(\tau_t^c; \theta)$. For notational simplicity, we denote the right-
 260 hand side by $\mathbf{u}_t = \{\mathbf{u}_t^0, \mathbf{u}_t^1, \dots, \mathbf{u}_t^H\} \in \mathbb{R}^{d \times (H+1)}$ ($\mathbf{u}_t^k \in \mathbb{R}^d$).³ We now formalize the concept of
 261 safety in flow matching using finite-time flow invariance.
 262

263 ³(14) is a control-affine system with drift $f(\tau_t^{c,k}) = \tilde{v}_t^k$ and input matrix $g = I$. Thus, at the waypoint
 264 level, the structure coincides with the standard control-affine system used in Section 2.2.
 265

270 **Definition 3 (Finite-Time Flow Invariance)** Let $b: \mathcal{D} \rightarrow \mathbb{R}$ be a C^1 function. The system (13) is
 271 finite-time flow invariant if there exists $t_f \in [0, 1]$ such that $b(\boldsymbol{\tau}_t^{c,k}) \geq 0$ for all $k \in \mathcal{H}, \forall t \geq t_f$.
 272

273 **Theorem 1 (Forward Invariance for SafeFlowMatcher)** Let $b: \mathcal{D} \rightarrow \mathbb{R}$ be a C^1 function, and de-
 274 fine the robust safety set $\mathcal{C}_\delta \triangleq \{\boldsymbol{\tau}^{c,k} \in \mathcal{D} \mid b(\boldsymbol{\tau}^{c,k}) \geq \delta\}$ for some $\delta > 0$. Suppose the system (13) is
 275 controlled by \mathbf{u}_t satisfying the following barrier certificate for $0 < \rho < 1, \epsilon > 0$:
 276

$$277 \nabla b(\boldsymbol{\tau}_t^{c,k})^\top \mathbf{u}_t^k + \epsilon \cdot \text{sgn}(b(\boldsymbol{\tau}_t^{c,k}) - \delta) |b(\boldsymbol{\tau}_t^{c,k}) - \delta|^\rho + w_t^k r_t^k \geq 0, \forall k \in \mathcal{H}, \forall t \in [0, 1]. \quad (15)$$

278 Here, $w_t^k: [0, 1] \rightarrow \mathbb{R}_{\geq 0}$ is a monotonically decreasing function with $w_t^k = 0$ for all $t \in [t_w, 1]$
 279 ($t_w \in [0, 1)$), and $r_t^k \geq 0$ is a slack variable. Then the flow matching (13) achieves finite-time flow
 280 invariance on \mathcal{C}_δ .
 281

282 The weights w_t^k serve as functions that relax the CBF constraint in the early refining phase, providing
 283 numerical stability by preventing infeasibility and reducing abrupt changes in the QP solution. Since
 284 w_t^k vanishes for $t \geq t_w$, the relaxation term has no effect afterwards, ensuring that the final path
 285 satisfies certified safety.

286 **Proposition 1 (Finite Convergence Time for SafeFlowMatcher)** Suppose Theorem 1 holds. Then
 287 for any initial path $\boldsymbol{\tau}_{t_w}^{c,k} \in \mathcal{D} \setminus \mathcal{C}_\delta$, the state path $\boldsymbol{\tau}_t^{c,k}$ converges to the safe set \mathcal{C}_δ within finite time
 288

$$289 \quad T \leq t_w + \frac{(\delta - b(\boldsymbol{\tau}_{t_w}^{c,k}))^{1-\rho}}{\epsilon(1-\rho)}, \quad (16)$$

292 and remains in the set thereafter.
 293

294 Proposition 1 allows us to select parameters ϵ and ρ to guarantee flow invariance on the robust safe
 295 set \mathcal{C}_δ before the time (16). The proofs of Theorem 1 and Proposition 1 are in Appendix C.

296 In order to enforce the invariance of the safety set \mathcal{C}_δ with minimum intervention during planning,
 297 we solve a quadratic program (QP) analogous to (8) at each sampling time t and planning step k :
 298

$$299 \quad \mathbf{u}_t^{k*}, r_t^{k*} = \arg \min_{\mathbf{u}_t^k, r_t^k} \|\mathbf{u}_t^k - \tilde{v}_t^k(\boldsymbol{\tau}_t^c; \theta)\|^2 + r_t^{k^2} \quad \text{subject to} \quad (15), \quad (17)$$

301 where \mathbf{u}_t^k and $\tilde{v}_t^k(\boldsymbol{\tau}_t^c; \theta)$ are defined in (14). Since the QP (17) is equivalent to a Euclidean projec-
 302 tion problem with linear inequalities, closed-form solutions are available when it has at most two
 303 inequalities (Luenberger, 1997; Boyd & Vandenberghe, 2004). Moreover, the computational time
 304 can be reduced further by decreasing the correction horizon T^c or balancing (T^p, T^c) , as discussed
 305 in Appendix F.1.

306 **Remark 1** The PC integrator brings $\boldsymbol{\tau}_0^c$ closer to the barrier boundary after the prediction phase.
 307 By Proposition 1, this improved initialization reduces the required convergence time, allowing us
 308 a wider range of choices for (ρ, ϵ) , and more stable control inputs. We empirically validate this in
 309 Appendix F.2.
 310

311 **Remark 2** The relaxation term is mainly necessary in environments where the planner is prone to
 312 becoming locally stuck due to complex safety constraints. In particular, it is essential in Maze2D,
 313 where the safe set is highly non-convex, leading to frequent local traps. In contrast, in relatively
 314 open or convex environments such as locomotion or robot manipulation tasks in our experiments,
 315 the relaxation is typically unnecessary. In such cases, the relaxation term w_t^k remains zero, and the
 316 slack variable r_t^k can be removed from (15).
 317

318 4 EXPERIMENTS

320 We evaluate SafeFlowMatcher through experiments designed to answer three key questions:
 321

- 322 1. Does SafeFlowMatcher outperform state-of-the-art generative model based safe planning
 323 baselines in terms of safety, planning performance, and efficiency?
- 324 2. Does SafeFlowMatcher really require a two-phase (prediction and correction) approach?

324
 325 3. How well can SafeFlowMatcher generalize to more complex and high-dimensional tasks
 326 (e.g., robot locomotion and manipulation)?

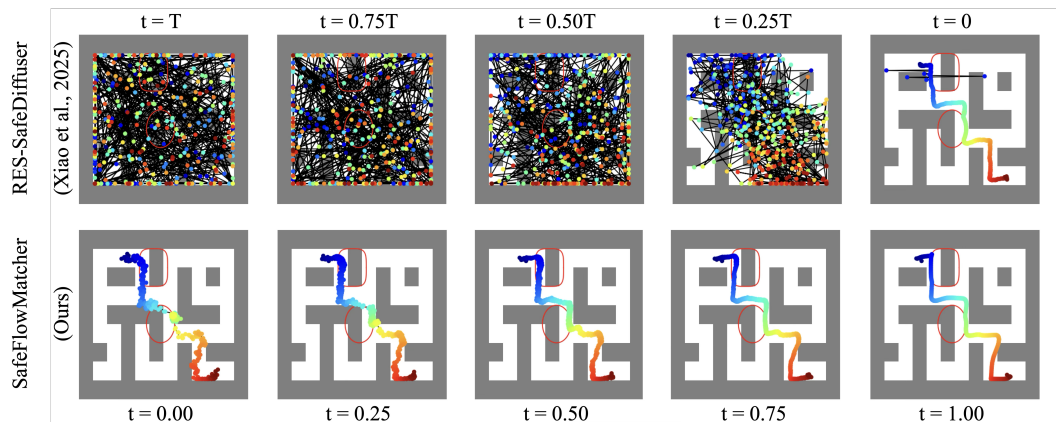
327 We conduct experiments on a variety of planning domains: (i) Maze navigation
 328 (maze-large-v1), (ii) OpenAI Gym locomotion (Walker2D-Medium-Expert-v2,
 329 Hopper-Medium-Expert-v2) (Brockman et al., 2016; Todorov et al., 2012), and (iii) a robot
 330 manipulation task (block stacking) (Janner et al., 2022).

331 To fairly evaluate our proposed method, we extend *SafeDiffuser* (Xiao et al., 2025) beyond its orig-
 332 inal DDPM sampler. We introduce three additional safety-aware variants. For the first and second
 333 variants, we adapt DDIM (Song et al., 2021a) into two versions, *SafeDDIM*($\eta=0.0$ & 1.0), which
 334 share the same weights as SafeDiffuser; here, η controls the level of sampling randomness. The
 335 last variant we develop is *SafeFM*, a flow-matching counterpart to SafeDiffuser which uses the
 336 same weights as SafeFlowMatcher, but enforces safety directly during sampling and without the
 337 prediction-correction integrator. When safety constraints are disabled, we drop the “Safe” prefix.
 338 Additional details on experimental settings are provided in Appendix E.1.

339 For safety, we report *Barrier Safety* (BS) per constraint, the minimum value of the barrier function b
 340 (which should remain non-negative), and *Trap Rate*, the rate of local trap occurrences. For planning
 341 quality, we measure the overall *Score*, the average path *Curvature* (κ), and the average path *Accel-
 342 eration* (a) over the planning horizon. For efficiency, we report *S-Time*, the computation time per
 343 sampling step during generation, and *T-Time*, the total computation time to generate an entire path.
 344 Formal definitions of the metrics are provided in Appendix E.2.

345 4.1 MAIN RESULTS ON MAZE2D NAVIGATION

346 We first present the main performance comparison in the Maze2D setting, as shown in Figure 3,
 347 where there are two safety constraints (red circles). Our results illustrate that SafeFlowMatcher
 348 generates smooth, efficient paths that effectively avoid obstacles, whereas baselines may produce
 349 unsafe, suboptimal, or computationally-expensive paths.



366 Figure 3: **Comparisons of the path generation process in Maze2D.** Red circles indicate the safety
 367 constraints the path should satisfy. (Top) RES-SafeDiffuser initializes samples all over the maze
 368 and converges to a path that has local traps. (Bottom) SafeFlowMatcher (ours) initializes from near
 369 target path after prediction phase, and converges to a higher-quality path with no local traps.⁴

370 As shown in Table 1, SafeFlowMatcher achieves the highest score while preserving safety, with
 371 almost no local traps. Local traps remain rare even with far more than two constraints; Appendix F.1
 372 shows the case with six constraints.

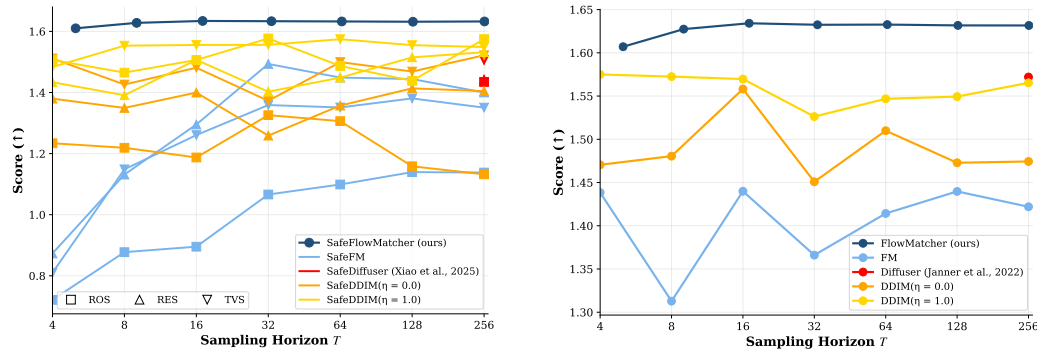
373 Moreover, Figure 4 demonstrates that our method consistently outperforms all baselines, both safety-
 374 enabled and -disabled versions, across all sampling horizons. As detailed in Appendix F.3, regarding

377 ⁴Diffusion-based samplers evolve backward on an interval $[0, T]$, whereas flow matching evolves forward
 378 on $[0, 1]$; a natural correspondence can be established by normalizing $T = 1$ and reversing time.

378 both safety and efficiency, our method also maintains 100% safety even at very short sampling horizons. Especially, when $T^c = 4$ and using the closed-form solution, our method achieves **50× faster**
379 T-Time than SafeDiffuser (0.023s vs. 1.208s), while SafeDiffuser still suffers from severe local
380 traps that lead to incomplete paths. When using the QP solver, SafeDiffuser completes generation in
381 9.998s, whereas SafeFlowMatcher completes generation in just 0.157s. Notably, the QP-based Safe-
382 FlowMatcher is still about **8× faster** than even the closed-form version of SafeDiffuser (1.208s),
383 while achieving high task performance. We further analyze the distributional drift introduced by
384 CBF-based corrections in Appendix F.4.
385

Method	BS1 (↑) (≥ 0)	BS2 (↑) (≥ 0)	Score (↑)	S-TIME (ms)	TRAP RATE	κ (↓)	a (↓)
Diffuser (Janner et al., 2022)	-0.825	-0.784	1.572±0.288	3.70	0%	77.04±4.30	86.68±3.81
DDIM($\eta = 0.0$)	-0.642	-0.902	1.474±0.106	3.63	0%	64.51±4.35	57.46±2.46
DDIM($\eta = 1.0$)	-0.595	-0.899	1.565±0.140	3.72	0%	64.21±5.00	57.15±1.96
FM	-1.000	-1.000	1.422±0.359	3.51	0%	52.09±22.02	33.96±22.95
FlowMatcher	-0.324	-0.904	1.632±0.003	3.51	0%	73.51±1.02	88.45±0.60
Truncation (Brockman et al., 2016)	-0.999	-0.999	0.978±0.128	19.51	100%	1118.21±1093.96	9.043e5±8.988e6
CG (Dhariwal & Nichol, 2021)	-0.996	-0.999	0.505±0.092	19.13	100%	949.63±1103.62	959.71±1846.58
CG-ε (Dhariwal & Nichol, 2021)	-0.998	-0.999	0.499±0.104	19.87	100%	1027.28±1124.70	1.202e9±1.1961e10
ROS-SafeDiffuser (Xiao et al., 2025)	0.010	0.010	1.435±0.502	4.67	100%	75.15±6.67	422.87±86.70
RES-SafeDiffuser (Xiao et al., 2025)	0.010	0.010	1.442±0.451	4.72	72%	80.30±13.06	398.17±1060.86
TVS-SafeDiffuser (Xiao et al., 2025)	-0.003	-0.003	1.506±0.405	4.78	69%	78.72±7.80	124.51±34.22
ROS-SafeDDIM($\eta = 0.0$)	0.010	0.010	1.132±0.556	4.79	100%	31.22±4.87	2073.84±1694.06
RES-SafeDDIM($\eta = 0.0$)	0.010	0.010	1.405±0.494	4.83	96%	43.23±3.41	1153.81±2040.98
TVS-SafeDDIM($\eta = 0.0$)	-0.026	-0.026	1.522±0.295	4.79	90%	42.56±3.39	575.73±371.83
ROS-SafeDDIM($\eta = 1.0$)	0.010	0.010	1.575±0.158	4.89	100%	56.30±2.93	668.17±69.19
RES-SafeDDIM($\eta = 1.0$)	0.010	0.010	1.532±0.331	4.82	86%	61.73±4.80	1584.00±8085.06
TVS-SafeDDIM($\eta = 1.0$)	-0.026	-0.026	1.549±0.304	4.74	65%	60.29±3.41	27.23±43.20
ROS-SafeFM	0.010	0.010	1.138±0.556	4.68	100%	23.57±8.34	1.317e4±9.931e4
RES-SafeFM	0.010	0.010	1.401±0.429	4.74	12%	61.17±19.52	6724.64±5.304e4
TVS-SafeFM	-0.002	-0.002	1.350±0.417	4.73	41%	60.29±3.41	768.71±2212.17
SafeFlowMatcher w/o relaxation (ours)	0.010	0.010	1.622±0.065	4.76	2%	71.73±3.54	108.43±167.36
SafeFlowMatcher (ours)	0.010	0.010	1.632±0.003	4.71	0%	69.19±1.02	91.90±0.77

402 Table 1: **Performance comparison of different methods.** we evaluated all methods over 100 inde-
403 pendent trials under identical settings. For all safety-aware methods, we set the robustness margin
404 to $\delta = 0.01$, meaning that a method is considered safe only if $b(\tau) \geq \delta$. This ensures robust rather
405 than marginal safety. FlowMatcher-variants use $T^p = 1$ and $T^c = 256$, and others use $T = 256$. The
406 closed-form CBF-QP computation takes 1.14 ms on average. All baselines are reproduced by us.



419 Figure 4: **Score versus sampling horizon T .** Left (safety on): SafeFlowMatcher attains the highest
420 score across all sampling horizons. Right (safety off): FlowMatcher (FM + PC integrator) also re-
421 mains more efficient than the other cases.

4.2 ABLATION STUDIES ON PC INTEGRATOR

424 **Effect of Using Two Phases.** To highlight the necessity of both the prediction and correction
425 phases, we discuss the results of FlowMatcher (prediction-only), SafeFM (correction-only), and
426 SafeFlowMatcher (PC integrator) in Table 1. The prediction-only behavior achieves good task per-
427 formance but lacks safety. Conversely, the correction-only behavior enforces safety from the
428 beginning but often fails to generate complete paths, resulting in a high trap rate. SafeFlowMatcher
429 combines the strengths of both phases, achieving superior performance while ensuring safety.

431 **Effect of Prediction Horizon (T^p).** We analyze how the prediction horizon T^p affects overall
432 performance while keeping the correction horizon fixed at $T^c = 256$. Table 2 reports the qualities

of fully generated paths and the total computation time across different values of T^p , and Figure 5 visualizes how increasing T^p shapes the predicted path before correction. As T^p increases, the path quality remains largely unchanged, while the computation cost increases due to additional prediction steps.

Table 2: **Effect of prediction horizon T^p .** We compare path quality metrics (score, curvature, and acceleration) and the total computation time, measured after one full path generation.

Prediction horizon (T^p)	1	2	4	8	16
Score (\uparrow)	1.632±0.008	1.520±0.340	1.468±0.434	1.404±0.538	1.632±0.003
T-TIME (s)	1.209	1.220	1.230	1.249	1.287
Curvature κ (\downarrow)	69.19±1.02	68.84±3.32	68.70±4.62	68.26±4.77	67.73±4.97
Acceleration a (\downarrow)	91.90±2.77	93.76±2.30	93.18±3.52	91.99±3.83	92.61±3.81

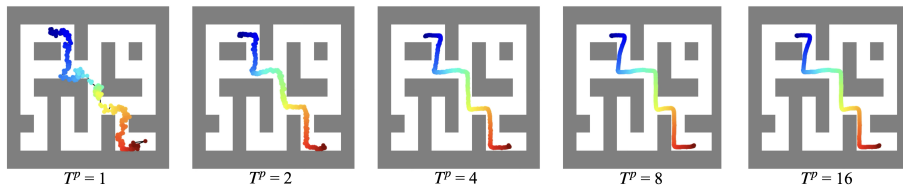


Figure 5: **Predicted paths under different prediction horizon T^p .** Each shows the predicted path after the prediction phase. As prediction horizon T^p increases, prediction error ε decreases.

Effect of Vanishing Time-Scale. We first analyze the role of the scaling constant α in VTFD (10). As shown in Table 3 and Figure 6, increasing α consistently reduces both curvature and acceleration, indicating that larger scaling factors suppress the prediction error more aggressively. This trend is consistent with the theoretical result from Lemma 3.

However, we observe that a larger α introduces bias in the final path. This effect is visible in Figure 6, where the red path region stays relatively stable up to a certain critical value but becomes increasingly distorted once α exceeds this threshold. In our Maze2D setup, this occurs around $\alpha \approx 2$. This shows that α should not simply be maximized in practice; instead, one can start from $\alpha = 1$ and increase it until we identify the point just before the sharp distortion begins.

Figure 7 shows how the score changes with increasing correction horizon T^c when $T^p = 1$. With vanishing time-scale, the score remains stable even as T^c grows, whereas removing the scaling causes the score to deteriorate steadily. Figure 8 provides the corresponding path visualization. With vanishing time-scale, the correction path moves from τ_0^c to τ_1^c along a straight direction. In contrast, without scaling, the path exhibits sharp drift near $t = 1$, and some segments of the path become largely distorted. These results demonstrate that vanishing time-scale is essential for preventing late-stage drift and maintaining stable refinement behavior.

Table 3: **Effect of scaling constant α .** Path qualities are measured after full generation.

Scaling constant α	1.0	1.5	2.0	2.5	3.0
Score (\uparrow)	1.623±0.005	1.629±0.004	1.632±0.008	1.618±0.033	1.572±0.058
Curvature κ (\downarrow)	85.10±3.73	83.91±2.00	69.28±1.04	55.16±0.83	44.08±0.62
Acceleration a (\downarrow)	173.22±5.62	123.49±1.86	92.05±0.59	71.89±0.42	58.05±0.24

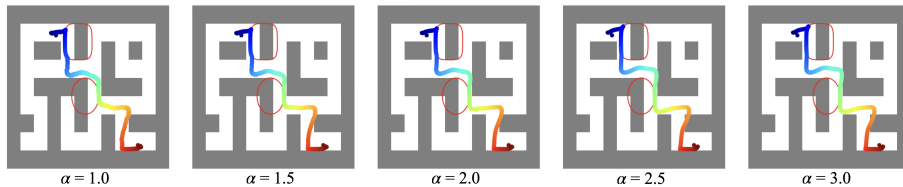


Figure 6: **Generated paths under different scaling constant α .** Each snapshot shows the fully generated path after the two phases. As the scaling constant α increases, the path becomes smoother but can be distorted.

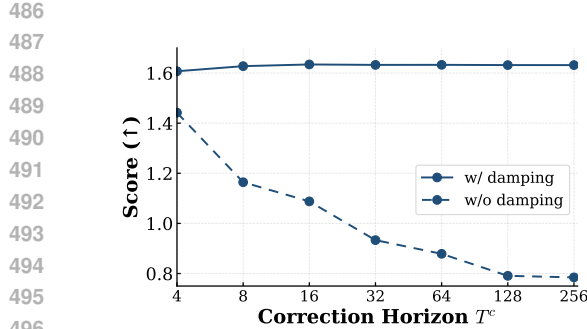


Figure 7: **Score with and without a vanishing time-scale.** When $T^p = 1$, as the correction horizon T^c increases, we see that the score decreases in the absence of vanishing time-scale.

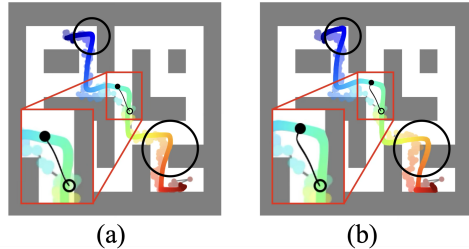


Figure 8: **Generation process with (a) and without (b) a vanishing time-scale.** The transparent path represents τ_0^c , the solid path represents τ_1^c . The black line represents the path τ_t^c from \circ to \bullet over the interval $t \in [0, 1]$. The path's segments in the black circles are largely distorted in the absence of a vanishing time-scale.

4.3 GENERALIZATION TO HIGH-DIMENSIONAL ROBOTIC TASKS

We evaluate the generalization capability of SafeFlowMatcher on high-dimensional robotic tasks, including two locomotion environments (Walker2D and Hopper) and a robot manipulation task (Block Stacking). Across all three tasks, SafeFlowMatcher attains the highest score while maintaining $BS \geq 0$, indicating that the PC integrator scales beyond static maze navigation. The detailed comparison across locomotion and manipulation tasks is summarized in Table 4. Note that the BS metric here is reported in a different way than in Table 1; here, BS is a binary indicator (yes or no) of whether safety is guaranteed (≥ 0) or not (< 0).

Table 4: **Performance on high-dimensional robotic tasks.** SafeFlowMatcher maintains its advantages in both locomotion and robot manipulation settings.

Category	Environment	Method	Score (↑)	BS (≥ 0)
Locomotion	Walker2D	SafeDiffuser (Xiao et al., 2025)	0.283 ± 0.135	Yes
		SafeFM	0.264 ± 0.127	Yes
		Ours	0.331 ± 0.021	Yes
	Hopper	SafeDiffuser (Xiao et al., 2025)	0.435 ± 0.068	Yes
		SafeFM	0.675 ± 0.312	Yes
		Ours	0.917 ± 0.026	Yes
Robot Manipulation	Block Stacking	SafeDiffuser (Xiao et al., 2025)	0.72 ± 0.055	Yes
		SafeFM	0.73 ± 0.056	Yes
		Ours	0.76 ± 0.053	Yes

5 CONCLUSION

We introduced *SafeFlowMatcher*, a planning framework that couples flow matching (FM) with CBF-certified safety by employing a two-phase *prediction–correction* integrator. On the path generation side, we proposed the vanishing time-scaled flow dynamics, which contracts the prediction error toward the target path. On the safety side, we established a finite-time convergence barrier certificate for the flow system to ensure forward invariance of a safe set. The approach generates a candidate path with the learned FM dynamics and then refines only the *executed* path under safety constraints. This decoupling preserves the native generative dynamics, avoids distributional drift from repeated interventions on latent states, and mitigates local trap failures near constraint boundaries. Empirically, SafeFlowMatcher attains faster, smoother, and safer paths than various diffusion- and FM-based baselines across maze navigation, locomotion, and robot manipulation tasks. Incorporating data-driven certificates is a promising direction for extending certified generative planning to more dynamic and complex environments.

540 **Reproducibility Statement.** All baseline results reported in this paper are fully reproduced by us
 541 using our own implementations or publicly available code, ensuring a fair and controlled compar-
 542 ison on the same hardware. To facilitate reproducibility, we provide anonymized source code for
 543 training and evaluation in the supplementary material. For fair comparisons under matched compu-
 544 tational budgets, our model architectures strictly adhere to those in prior work (Janner et al., 2022;
 545 Xiao et al., 2025) and their official implementations (Code: <https://github.com/jannerm/diffuser>,
 546 <https://github.com/Weixy21/SafeDiffuser>). Our experiments are conducted on the Maze2D environ-
 547 ment, locomotion tasks (Hopper, Walker2d) and a robot manipulation (block stacking). All hyper-
 548 parameters for training and evaluation, including optimizer settings, learning rates, and rollout con-
 549 figurations, are detailed in Appendix E. For each experimental setting, we perform 100 independent
 550 trials and report the mean and standard deviation across these runs in Table 1 and Table 4. All exper-
 551 iments were run on a machine equipped with an AMD EPYC9354 CPU and an NVIDIA RTX4090
 552 (24GB) GPU. Additional ablation studies are provided in Appendix F.

553 **REFERENCES**

555 Hossein Abdi, Golnaz Raja, and Reza Ghachcheloo. Safe control using vision-based control barrier
 556 function (v-cbf). In *IEEE International Conference on Robotics and Automation*, pp. 782–788.
 557 IEEE, 2023.

558 Ayush Agrawal and Koushil Sreenath. Discrete control barrier functions for safety-critical control of
 559 discrete systems with application to bipedal robot navigation. In *Robotics: Science and Systems*,
 560 volume 13, pp. 1–10. Cambridge, MA, USA, 2017.

561 Aaron D Ames, Xiangru Xu, Jessy W Grizzle, and Paulo Tabuada. Control barrier function based
 562 quadratic programs for safety critical systems. *IEEE Transactions on Automatic Control*, 62(8):
 563 3861–3876, 2016.

564 Aaron D Ames, Samuel Coogan, Magnus Egerstedt, Gennaro Notomista, Koushil Sreenath, and
 565 Paulo Tabuada. Control barrier functions: Theory and applications. In *2019 18th European
 566 control conference (ECC)*, pp. 3420–3431. Ieee, 2019.

567 Sanjay P Bhat and Dennis S Bernstein. Finite-time stability of continuous autonomous systems.
 568 *SIAM Journal on Control and optimization*, 38(3):751–766, 2000.

569 Stephen P Boyd and Lieven Vandenberghe. *Convex optimization*. Cambridge university press, 2004.

570 Max Braun, Noémie Jaquier, Leonel Rozo, and Tamim Asfour. Riemannian flow matching policy
 571 for robot motion learning. In *2024 IEEE/RSJ International Conference on Intelligent Robots and
 572 Systems (IROS)*, pp. 5144–5151. IEEE, 2024.

573 Greg Brockman, Vicki Cheung, Ludwig Pettersson, Jonas Schneider, John Schulman, Jie Tang, and
 574 Wojciech Zaremba. Openai gym. *CoRR*, abs/1606.01540, 2016.

575 Joao Carvalho, An T Le, Mark Baierl, Dorothea Koert, and Jan Peters. Motion planning diffusion:
 576 Learning and planning of robot motions with diffusion models. In *2023 IEEE/RSJ International
 577 Conference on Intelligent Robots and Systems (IROS)*, pp. 1916–1923. IEEE, 2023.

578 Chang Chen, Fei Deng, Kenji Kawaguchi, Caglar Gulcehre, and Sungjin Ahn. Simple hierarchical
 579 planning with diffusion. *CoRR*, abs/2401.02644, 2024.

580 Eugenio Chisari, Nick Heppert, Max Argus, Tim Welschehold, Thomas Brox, and Abhinav Valada.
 581 Learning robotic manipulation policies from point clouds with conditional flow matching. In *8th
 582 Annual Conference on Robot Learning*, 2024.

583 Ryan K Cosner, Andrew W Singletary, Andrew J Taylor, Tamas G Molnar, Katherine L Bouman,
 584 and Aaron D Ames. Measurement-robust control barrier functions: Certainty in safety with un-
 585 certainty in state. In *2021 IEEE/RSJ International Conference on Intelligent Robots and Systems
 586 (IROS)*, pp. 6286–6291. IEEE, 2021.

587 Prafulla Dhariwal and Alexander Nichol. Diffusion models beat GANs on image synthesis. *Ad-
 588 vances in neural information processing systems*, 34:8780–8794, 2021.

594 Ruiqi Feng, Changlei Yu, Wenhao Deng, Peiyan Hu, and Tailin Wu. On the guidance of flow
 595 matching. In *Forty-second International Conference on Machine Learning*, 2025.

596

597 Marvin Harms, Mihir Kulkarni, Nikhil Khedekar, Martin Jacquet, and Kostas Alexis. Neural control
 598 barrier functions for safe navigation. In *2024 IEEE/RSJ International Conference on Intelligent
 599 Robots and Systems (IROS)*, pp. 10415–10422. IEEE, 2024.

600 Jonathan Ho and Tim Salimans. Classifier-free diffusion guidance. In *NeurIPS 2021 Workshop on
 601 Deep Generative Models and Downstream Applications*, 2021.

602

603 Jonathan Ho, Ajay Jain, and Pieter Abbeel. Denoising diffusion probabilistic models. *Advances in
 604 neural information processing systems*, 33:6840–6851, 2020.

605 Kai-Chieh Hsu, Haimin Hu, and Jaime F Fisac. The safety filter: A unified view of safety-critical
 606 control in autonomous systems. *Annual Review of Control, Robotics, and Autonomous Systems*,
 607 7, 2023.

608 Michael Janner, Yilun Du, Joshua Tenenbaum, and Sergey Levine. Planning with diffusion for
 609 flexible behavior synthesis. In *International Conference on Machine Learning*, pp. 9902–9915.
 610 PMLR, 2022.

611

612 Zhuozhu Jian, Zihong Yan, Xuanang Lei, Zihong Lu, Bin Lan, Xueqian Wang, and Bin Liang.
 613 Dynamic control barrier function-based model predictive control to safety-critical obstacle-
 614 avoidance of mobile robot. In *2023 IEEE International Conference on Robotics and Automation
 615 (ICRA)*, pp. 3679–3685. IEEE, 2023.

616 Hassan K Khalil and Jessy W Grizzle. *Nonlinear systems*, volume 3. Prentice hall Upper Saddle
 617 River, NJ, 2002.

618

619 Jeeseop Kim, Jaemin Lee, and Aaron D Ames. Safety-critical coordination for cooperative legged
 620 locomotion via control barrier functions. In *2023 IEEE/RSJ International Conference on Intelli-
 621 gent Robots and Systems (IROS)*, pp. 2368–2375. IEEE, 2023.

622 Anqi Li, Li Wang, Pietro Pierpaoli, and Magnus Egerstedt. Formally correct composition of coor-
 623 dinated behaviors using control barrier certificates. In *2018 IEEE/RSJ International Conference
 624 on Intelligent Robots and Systems (IROS)*, pp. 3723–3729. IEEE, 2018.

625

626 Qiayuan Liao, Zhongyu Li, Akshay Thirugnanam, Jun Zeng, and Koushil Sreenath. Walking in
 627 narrow spaces: Safety-critical locomotion control for quadrupedal robots with duality-based opti-
 628 mization. In *2023 IEEE/RSJ International Conference on Intelligent Robots and Systems (IROS)*,
 629 pp. 2723–2730. IEEE, 2023.

630 Lars Lindemann, Alexander Robey, Lejun Jiang, Satyajeet Das, Stephen Tu, and Nikolai Matni.
 631 Learning robust output control barrier functions from safe expert demonstrations. *IEEE Open
 632 Journal of Control Systems*, 3:158–172, 2024.

633 Yaron Lipman, Ricky T. Q. Chen, Heli Ben-Hamu, Maximilian Nickel, and Matthew Le. Flow
 634 matching for generative modeling. In *The Eleventh International Conference on Learning Repre-
 635 sentations*, 2023.

636

637 Jianwei Liu, Maria Stamatopoulou, and Dimitrios Kanoulas. Dipper: Diffusion-based 2d path plan-
 638 ner applied on legged robots. In *2024 IEEE International Conference on Robotics and Automation
 639 (ICRA)*, pp. 9264–9270. IEEE, 2024.

640 Luping Liu, Yi Ren, Zhijie Lin, and Zhou Zhao. Pseudo numerical methods for diffusion models on
 641 manifolds. In *International Conference on Learning Representations*, 2022.

642 Kehan Long, Cheng Qian, Jorge Cortés, and Nikolay Atanasov. Learning barrier functions with
 643 memory for robust safe navigation. *IEEE Robotics and Automation Letters*, 6(3):4931–4938,
 644 2021.

645

646 Kehan Long, Vikas Dhiman, Melvin Leok, Jorge Cortés, and Nikolay Atanasov. Safe control syn-
 647 thesis with uncertain dynamics and constraints. *IEEE Robotics and Automation Letters*, 7(3):
 7295–7302, 2022.

648 Cheng Lu, Yuhao Zhou, Fan Bao, Jianfei Chen, Chongxuan Li, and Jun Zhu. Dpm-solver: A fast
 649 ode solver for diffusion probabilistic model sampling in around 10 steps. *Advances in neural*
 650 *information processing systems*, 35:5775–5787, 2022.

651

652 David G Luenberger. *Optimization by vector space methods*. John Wiley & Sons, 1997.

653

654 Mitio Nagumo. Über die lage der integralkurven gewöhnlicher differentialgleichungen. *Proceedings*
 655 *of the physico-mathematical society of Japan. 3rd Series*, 24:551–559, 1942.

656

657 Ahmed H Qureshi, Anthony Simeonov, Mayur J Bency, and Michael C Yip. Motion planning net-
 658 works. In *2019 International Conference on Robotics and Automation (ICRA)*, pp. 2118–2124.
 659 IEEE, 2019.

660

661 Alexander Robey, Haimin Hu, Lars Lindemann, Hanwen Zhang, Dimos V Dimarogonas, Stephen
 662 Tu, and Nikolai Matni. Learning control barrier functions from expert demonstrations. In *2020*
 663 *59th IEEE Conference on Decision and Control (CDC)*, pp. 3717–3724. Ieee, 2020.

664

665 Jiaming Song, Chenlin Meng, and Stefano Ermon. Denoising diffusion implicit models. In *9th*
 666 *International Conference on Learning Representations, ICLR 2021, Virtual Event, Austria, May*
 667 *3-7, 2021*. OpenReview.net, 2021a.

668

669 Yang Song, Jascha Sohl-Dickstein, Diederik P Kingma, Abhishek Kumar, Stefano Ermon, and Ben
 670 Poole. Score-based generative modeling through stochastic differential equations. In *Inter-
 671 national Conference on Learning Representations*, 2021b.

672

673 Mohit Srinivasan, Samuel Coogan, and Magnus Egerstedt. Control of multi-agent systems with
 674 finite time control barrier certificates and temporal logic. In *2018 IEEE Conference on Decision*
 675 *and Control (CDC)*, pp. 1991–1996. IEEE, 2018.

676

677 Mohit Srinivasan, Amogh Dabholkar, Samuel Coogan, and Patricio A Vela. Synthesis of control
 678 barrier functions using a supervised machine learning approach. In *2020 IEEE/RSJ International*
 679 *Conference on Intelligent Robots and Systems (IROS)*, pp. 7139–7145. Ieee, 2020.

680

681 Emanuel Todorov, Tom Erez, and Yuval Tassa. Mujoco: A physics engine for model-based control.
 682 In *2012 IEEE/RSJ International Conference on Intelligent Robots and Systems*, pp. 5026–5033,
 683 2012. doi: 10.1109/IROS.2012.6386109.

684

685 Kim P Wabersich, Andrew J Taylor, Jason J Choi, Koushil Sreenath, Claire J Tomlin, Aaron D Ames,
 686 and Melanie N Zeilinger. Data-driven safety filters: Hamilton-jacobi reachability, control barrier
 687 functions, and predictive methods for uncertain systems. *IEEE Control Systems Magazine*, 43(5):
 688 137–177, 2023.

689

690 Li Wang, Aaron D Ames, and Magnus Egerstedt. Safety barrier certificates for collisions-free mul-
 691 tirobot systems. *IEEE Transactions on Robotics*, 33(3):661–674, 2017.

692

693 Wei Xiao, Tsun-Hsuan Wang, Chuang Gan, Ramin Hasani, Mathias Lechner, and Daniela Rus.
 694 Safediffuser: Safe planning with diffusion probabilistic models. In *The Thirteenth International*
 695 *Conference on Learning Representations*, 2025.

696

697 Zebin Xing, Xingyu Zhang, Yang Hu, Bo Jiang, Tong He, Qian Zhang, Xiaoxiao Long, and Wei
 698 Yin. Goalflow: Goal-driven flow matching for multimodal trajectories generation in end-to-end
 699 autonomous driving. In *Proceedings of the IEEE/CVF Conference on Computer Vision and Pat-
 700 tern Recognition (CVPR)*, pp. 1602–1611, June 2025.

701

702 Brian Yang, Huangyuan Su, Nikolaos Gkanatsios, Tsung-Wei Ke, Ayush Jain, Jeff Schneider, and
 703 Katerina Fragkiadaki. Diffusion-es: Gradient-free planning with diffusion for autonomous and
 704 instruction-guided driving. In *Proceedings of the IEEE/CVF conference on computer vision and*
 705 *pattern recognition*, pp. 15342–15353, 2024.

706

707 Sean Ye and Matthew C Gombolay. Efficient trajectory forecasting and generation with conditional
 708 flow matching. In *2024 IEEE/RSJ International Conference on Intelligent Robots and Systems*
 709 *(IROS)*, pp. 2816–2823. IEEE, 2024.

702 Fan Zhang and Michael Gienger. Robot manipulation with flow matching. In *CoRL 2024 Workshop*
703 *on Mastering Robot Manipulation in a World of Abundant Data*, 2024.
704

705 Qinsheng Zhang and Yongxin Chen. Fast sampling of diffusion models with exponential integrator.
706 In *NeurIPS 2022 Workshop on Score-Based Methods*, 2022.

707
708
709
710
711
712
713
714
715
716
717
718
719
720
721
722
723
724
725
726
727
728
729
730
731
732
733
734
735
736
737
738
739
740
741
742
743
744
745
746
747
748
749
750
751
752
753
754
755

756 A ADDITIONAL RELATED WORK ON CONTROL BARRIER FUNCTIONS
757

758 Control Barrier Functions have been developed and extended in a wide range of directions, and
759 existing results show that CBF-based safety filter does not rely on perfectly known, smooth, or
760 analytically specified safety sets. Discrete-time CBFs have been applied to hybrid locomotion and
761 time-varying safety constraints (Agrawal & Sreenath, 2017), and duality-based DCBF methods en-
762 able safe control even with nonsmooth, polytopic, or nonconvex obstacle geometries (Liao et al.,
763 2023). Perception noise and state-estimation uncertainty can be handled using measurement-robust
764 and probabilistic CBF formulations (Cosner et al., 2021; Long et al., 2022). Moreover, CBFs have
765 been extended to dynamic-obstacle environments, explicitly incorporating obstacle motion predic-
766 tion and enabling real-time avoidance of moving obstacles (Jian et al., 2023).

767 In addition to analytic formulations, a growing line of work develops learning-based CBFs that
768 construct safety certificates directly from data rather than hand-crafted functions. These methods
769 learn barrier functions from RGB-D observations (Abdi et al., 2023), LiDAR scans (Srinivasan
770 et al., 2020; Long et al., 2021; Harms et al., 2024), or expert demonstrations (Robey et al., 2020;
771 Lindemann et al., 2024), enabling implicit representations of safety sets in dynamic and unstructured
772 environments. While SafeFlowMatcher currently leverages analytic CBFs, its correction phase only
773 requires evaluating a barrier constraint, making the framework compatible with these learned or
774 perception-driven CBFs.

775 Beyond their theoretical development, CBF-based safety filters have also been applied across a wide
776 range of robotic domains. They have seen successful use in autonomous driving (Ames et al., 2016),
777 legged locomotion (Kim et al., 2023), and multi-robot coordination (Wang et al., 2017).

778 B THEORETICAL AND EMPIRICAL SUPPORT FOR THE CORRECTION PHASE
779

780 B.1 EMPIRICAL VALIDATION OF THE PREDICTION ERROR ASSUMPTION IN LEMMA 2

781 Lemma 2 and Lemma 3 assume that the prediction error ε follows a symmetric, zero-mean distribu-
782 tion in a neighborhood around the target path. We empirically validate this assumption by evaluating
783 the distribution of ε under different prediction horizons $T^p \in \{1, 2, 4, 8, 16, 32\}$ in the Maze2D en-
784 vironment. For each configuration, we generate 1,000 predicted paths, resulting in a total of 384,000
785 waypoints, and evaluated the prediction error with respect to a high-accuracy FM solution τ_1^* , which
786 is computed using the Dormand-Prince 5(4) method (Dorpi5) with 256 steps.

787 Figure 9 visualizes our results. Across all values of T_p , the distribution of ε remains centered at zero
788 and exhibits symmetry, directly supporting the symmetric zero-mean (Gaussian-like) assumption
789 used in both lemmas. Validating whether this assumption still holds for higher-dimensional, complex
790 tasks is a subject of future work. However, we anticipate that while the final refined path may be
791 biased if the prediction error is biased, overall safety is still unaffected because the CBF-QP enforces
792 forward invariance regardless of any bias. Moreover, if the bias is heavy-tailed, the local strong
793 convexity of $-\log p_\varepsilon$ becomes weaker, which may slow down the contraction rate in the correction
794 phase. Again, this only affects path refinement speed, not safety guarantees, and increasing α to
795 introduce deliberate path distortion against the error (see Table 3 and Figure 6) might help the
796 prediction error reduction.

797 B.2 PROOFS OF LEMMA 2 AND LEMMA 3
798800 **Proof of Lemma 2.**

801 Let $\phi_t(\varepsilon) = \tau_1 + \delta\varepsilon$, where $\delta \triangleq 1 - t$. We have pushforward of p_ε under ϕ_t :

$$802 p_t(\tau | \tau_1) = [\phi_t]_\# p_\varepsilon(\varepsilon) = p_\varepsilon(\phi_t^{-1}(\tau)) \det \left[\frac{\partial \phi_t^{-1}}{\partial \tau}(\tau) \right] = \frac{1}{\delta^{d(H+1)}} p_\varepsilon \left(\frac{\tau - \tau_1}{\delta} \right)$$

803 By Bayes' rule,

$$804 p(\tau_1 | \tau_t^c) \propto p_1(\tau_1) p_\varepsilon \left(\frac{\tau_t^c - \tau_1}{\delta} \right).$$

805 Since $-\log p_\varepsilon(z)$ is C^2 near 0 with Hessian $A \succ 0$ by the assumption,

$$806 -\log p_\varepsilon(z) = \frac{1}{2} z^\top A z + O(\|z\|^3).$$

810 Let $y = \tau_1 - \tau_t^c$. Substituting $z = y/\delta$ yields the posterior energy
 811

$$812 \quad \Phi_\delta(y) = \frac{1}{2\delta^2} y^\top A y - \log p_1(\tau_t^c + y) + O(1).$$

813 The quadratic term dominates as $\delta \rightarrow 0$ ($t \rightarrow 1$), so the posterior concentrates in an $O(\delta)$ neighbor-
 814 hood of τ_t^c .
 815

816 The stationarity condition $\nabla \Phi_\delta(y) = 0$ gives
 817

$$818 \quad \frac{1}{\delta^2} A y - \nabla \log p_1(\tau_t^c + y) = 0.$$

820 Taylor expanding $\nabla \log p_1$ at τ_t^c shows $y = O(\delta^2)$. Thus the posterior mode is
 821

$$822 \quad \hat{\tau}_1 = \tau_t^c + \delta^2 A^{-1} \nabla \log p_1(\tau_t^c) + O(\delta^3).$$

823 Laplace's approximation then yields the same expansion for the posterior mean:
 824

$$825 \quad \mathbb{E}[\tau_1 | \tau_t^c] = \tau_t^c + \delta^2 A^{-1} \nabla \log p_1(\tau_t^c) + O(\delta^3).$$

826 Under the assumption, we have $\tau_t^c = \tau_1^* + \delta \varepsilon$ with $\|\varepsilon\| = O(1)$,
 827

$$828 \quad \mathbb{E}[\tau_1 | \tau_t^c] = \tau_1^* + \delta \varepsilon + O(\delta^2) = \tau_1^* + O(\delta).$$

829 This proves Lemma 2.
 830

831 Proof of Lemma 3.

832 If the flow dynamics follow the vanishing time-scaled flow dynamics (10), then we have:
 833

$$834 \quad \dot{\tau}_t^c = \alpha(1-t) v_t(\tau_t^c; \theta) = \alpha(\mathbb{E}[\tau_1 | \tau_t^c] - \tau_t^c).$$

835 Let $\mathbf{e}_t \triangleq \tau_t^c - \tau_1^* \in \mathbb{R}^{d \times (H+1)}$, and denote its k -th column by $e_{k,t} \in \mathbb{R}^d$. By Lemma 2, $\mathbb{E}[\tau_1 | \tau_t^c] = \tau_1^* + O(1-t)$ as $t \rightarrow 1$, hence we have
 836

$$837 \quad \dot{e}_{k,t} = -\alpha e_{k,t} + O(1-t).$$

838 Solving with an integrating factor gives
 839

$$840 \quad e_{k,t} = e^{-\alpha t} e_{k,0} + \alpha e^{-\alpha t} \int_0^t e^{\alpha s} O(1-s) ds = (e_{k,0} + O(1)) e^{-\alpha t} + O((1-t)^2).$$

841 Combining the column vectors again yields the form
 842

$$843 \quad \mathbf{e}_t = (\mathbf{e}_0 + O(1)) e^{-\alpha t} + O((1-t)^2), \quad \mathbf{e}_0 = \varepsilon.$$

844 which proves Lemma 3.
 845

846 C PROOF OF THEOREM 1 AND PROPOSITION 1

847 We drop the superscript c for simplicity, and choose the Lyapunov candidate function $V(\tau_t^k) \triangleq$
 848 $\max(\delta - b(\tau_t^k), 0)$. Since $w(t) = 0$ for all $t \geq t_w$, the barrier inequality (15) reduces on $[t_w, 1]$ to
 849

$$850 \quad \dot{b}(\tau_t^k) + \epsilon \cdot \text{sgn}(b(\tau_t^k) - \delta) |b(\tau_t^k) - \delta|^\rho \geq 0.$$

851 **Case 1:** If $\tau_{t_w}^k \in \mathcal{C}_\delta$ (i.e., $b(\tau_{t_w}^k) \geq \delta$), then $V(\tau_{t_w}^k) = 0$. For all $t \geq t_w$, if $b(\tau_t^k) > \delta$ we have
 852 $V(\tau_t^k) = 0$. If $b(\tau_t^k) = \delta$, the barrier inequality (15) with $\text{sgn}(0) = 0$ reduces to $\dot{b}(\tau_t^k) \geq 0$, so the
 853 path cannot exit \mathcal{C}_δ by Nagumo's principle (Nagumo, 1942)⁵. Therefore $V(\tau_t^k) = 0$ for all $t \geq t_w$,
 854 which implies $\tau_t^k \in \mathcal{C}_\delta$; the system stays in \mathcal{C}_δ .
 855

856 **Case 2:** If $\tau_{t_w}^k \notin \mathcal{C}_\delta$ (i.e., $b(\tau_{t_w}^k) < \delta$), then $V(\tau_t^k) = \delta - b(\tau_t^k) > 0$. The following finite-stability
 857 condition holds
 858

$$859 \quad \dot{V}(\tau_t^k) = -\dot{b}(\tau_t^k) \leq -\epsilon(\delta - b(\tau_t^k))^\rho = -\epsilon V(\tau_t^k)^\rho.$$

860 ⁵Nagumo's theorem states that if the vector field at the boundary lies in the tangent cone of a set, then the
 861 set is forward invariant.
 862

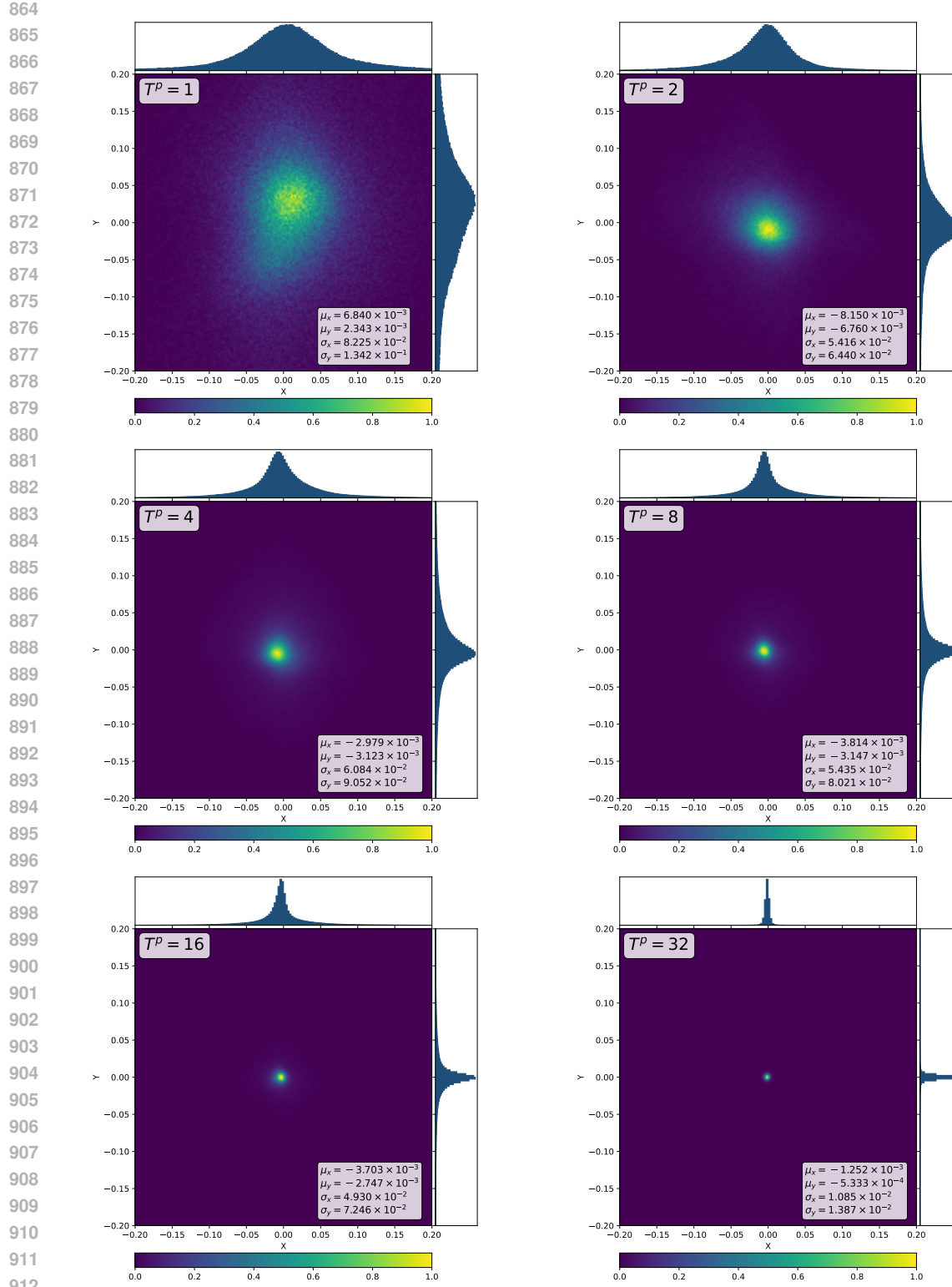


Figure 9: **Empirical distribution of the prediction error ε over prediction horizon T^p .** The six subfigures correspond to $T^p = 1, 2, 4, 8, 16, 32$ (from top-left to bottom-right). Each subplot visualizes the joint density of $(\varepsilon_x, \varepsilon_y)$ with its marginal distributions. As T^p increases, the error distribution becomes more concentrated around zero while maintaining symmetry, validating the symmetric zero-mean assumption used in Lemma 2 and Lemma 3.

918 Define the comparison system
 919

$$\dot{\phi}(t) = -\epsilon\phi(t)^\rho, \phi(t_w) = V(\tau_{t_w}^k).$$

920 By the Comparison Lemma (See Lemma 3.4 in Khalil & Grizzle (2002)), we have:
 921

$$V(\tau_t^k) \leq \phi(t), \forall t \geq t_w.$$

922 The solution $\phi(t)$ is
 923

$$\phi(t) = (V(\tau_{t_w}^k)^{1-\rho} - (1-\rho)\epsilon(t-t_w))^{\frac{1}{1-\rho}}, \text{ for } t \geq t_w.$$

924 Thus,
 925

$$V(\tau_t^k) \leq (V(\tau_{t_w}^k)^{1-\rho} - (1-\rho)\epsilon(t-t_w))^{\frac{1}{1-\rho}}.$$

926 Hence, the state reaches the robust safe set \mathcal{C}_δ in finite time T that satisfies $V(\tau_t^k) \leq \phi(T) = 0$.
 927 Moreover, we get the finite convergence time,
 928

$$T = t_w + \frac{V(\tau_{t_w}^k)^{1-\rho}}{\epsilon(1-\rho)} = t_w + \frac{(\delta - b(\tau_{t_w}^k))^{1-\rho}}{\epsilon(1-\rho)}.$$

929 Therefore, for all $t \geq T$, we have $V(\tau_t^k) \leq 0$, implying $\mathbf{x} \in \mathcal{C}_\delta$. This completes the proofs of both
 930 Theorem 1 and Proposition 1.
 931

932 D DIFFERENCES IN LOCAL TRAP DEFINITIONS

933 We clarify the difference between the local trap definition used
 934 in our SafeFlowMatcher and that of the baseline method SafeD-
 935 iffuser (Xiao et al., 2025).
 936

937 **Definition 4 (Local Trap in SafeDiffuser)** *A local trap problem
 938 occurs during the planning process if there exists $k \in \mathcal{H}$ such that
 939 $b(\tau_1^k) = 0$ and $\|\tau_1^k - \tau_1^{k-1}\| > \zeta$, where $\zeta > 0$ is a user-defined
 940 threshold depending on the planning environment.*

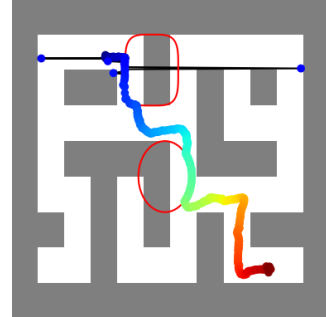
941 In contrast, our definition of a local trap in SafeFlowMatcher re-
 942 moves the condition $b(\tau_1^k) = 0$ and instead considers only the
 943 abrupt discontinuity in the path. The reason for relaxing the con-
 944 dition is illustrated in Figure 10. In this example, the generated path
 945 is incomplete due to overly strong or early intervention of the CBF.
 946 However, since the waypoints do not strictly lie on the boundary
 947 (i.e., $b(\tau_1^k) \neq 0$), the original SafeDiffuser definition fails to detect
 948 this failure as a local trap. Therefore, we generalize the definition to
 949 capture a wider class of failure cases.
 950

951 E EXPERIMENTAL DETAILS

952 E.1 EXPERIMENTAL SETUP

953 All CBF constraints are enforced via the closed-form projection of the CBF-QP in (17). For each
 954 model family, the safety-enabled variants reuse the same trained weights as their safety-disabled
 955 counterparts. Specifically, SafeDiffuser and SafeDDIM share the weights trained for Diffuser and
 956 DDIM, respectively, while SafeFM and SafeFlowMatcher share the weights trained for FM and
 957 FlowMatcher. All experiments are run using an AMD EPYC 9354 CPU and an NVIDIA RTX 4090
 958 GPU (24GB).
 959

960 **Maze2D.** To match the total amount of training data used in Diffuser (Janner et al., 2022), we
 961 first swept across several batch sizes while fixing the total number of samples processed during
 962 training to 6.4×10^7 . As shown in Table 5, both Diffuser and FM performed best or on par at
 963 batch size 128, so for all models and Maze2D experiments, we used batch size 128. Other training
 964



965 **Figure 10: Local trap occurring away from the safety
 966 boundary.** Although some waypoints do not violate con-
 967 straints (i.e., $b(\tau_t^k) > 0$), it fails to reach the goal.
 968 Our definition considers such cases as local traps, while the
 969 original definition does not.

and inference hyperparameters are shown in Tables 6. For the correction phase, we set the scaling constant to $\alpha = 2$, and use $(\delta, \varepsilon, \rho) = (0.01, 0.5, 0.9)$ for the CBF parameters. Additionally, for the relaxation schedule, t_w is chosen according to the correction horizon T^c . Specifically, we use $t_w \in \{0, 0.5, 0.75, 0.9, 0.9, 0.9, 0.99\}$ for $T^c \in \{4, 8, 16, 32, 64, 128, 256\}$, respectively. The relaxation function is defined as $w_t^k = 200(1 - e^{3(t/t_w-1)})$ for $t \leq t_w$, and $w_t^k = 0$ otherwise. For Maze2D, the planner is conditioned on the start and goal state observations, which are provided as the condition for each rollout.

Table 5: Scores by batch size for Maze2D for both Diffuser and FM.

Method	16	32	64	128	256
FlowMatcher	1.631 ± 0.003	1.628 ± 0.002	1.615 ± 0.031	1.631 ± 0.003	1.523 ± 0.196
Diffuser (Janner et al., 2022)	1.503 ± 0.424	1.438 ± 0.500	1.516 ± 0.316	1.537 ± 1.537	1.536 ± 0.338

Locomotion. Following the observations from Maze2D, we also train all locomotion models using a batch size of 128. SafeFlowMatcher, SafeFM, and SafeDiffuser share the same hyperparameter settings, summarized in Table 7. To provide score-based guidance to all flow-matching based methods, including SafeFM and SafeFlowMatcher, we apply a simple covariance-aware guidance $g^{\text{cov-A}}$ with scale 1.0, following prior work (Feng et al., 2025). During planning, we condition the model at each environment step on the current state observation and use the task score as a guidance signal to encourage forward progress.



(a) Walker2D planning result with SafeFlowMatcher.



(b) Hopper planning result with SafeFlowMatcher.

Figure 11: **SafeFlowMatcher on locomotion tasks.** Planning results for Walker2D (top) and Hopper (bottom). In both figures, the red horizontal line indicates the roof height h_r in the CBF barrier function ($z \leq h_r$) used in the BS metric (Appendix E.2).

Robot Manipulation (Block-Stacking). For the block stacking task, we followed the training parameters from Diffuser Janner et al. (2022) (batch size 32 with 2-step gradient accumulation, equivalent to batch size 64 without accumulation), rather than 128, while maintaining the number of training steps for training SafeFlowMatcher (SafeFM sharing weights with SafeFlowMatcher) and SafeDiffuser. Other hyperparameter values and conditions are shown in Table 8. For the block stacking task, the condition includes the initial robot joint configuration together with the observed states of the four blocks.

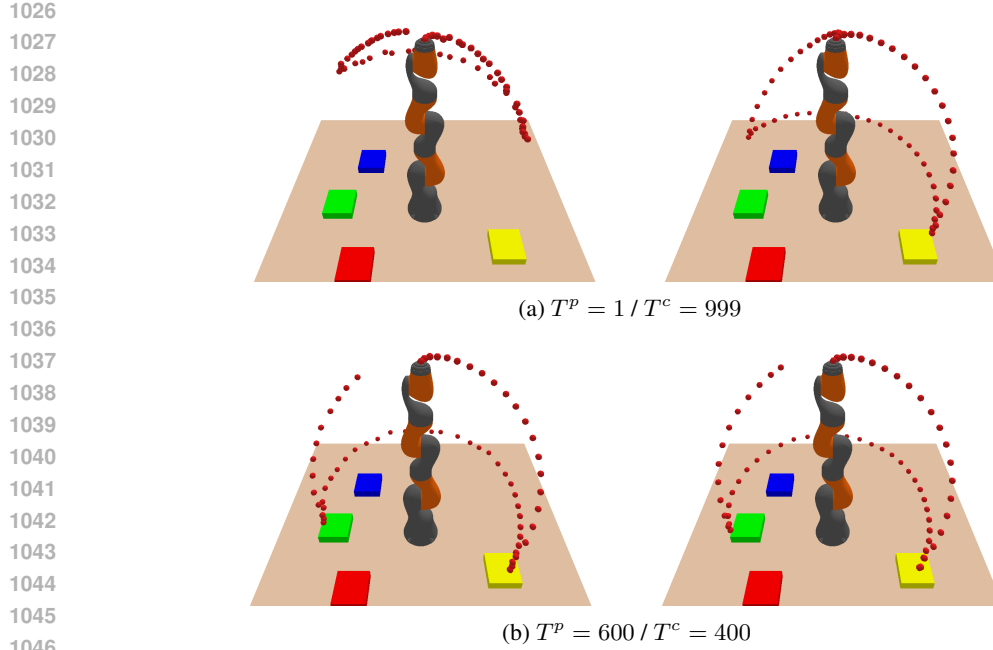


Figure 12: **Block stacking visual comparison based on the prediction and correction horizons.** For each subfigure, the left shows the predicted path τ_1^p and the right shows the corrected path τ_1^c . Under the same planning horizon $H = 128$, we compare different allocations of T^p and T^c . In (a), using $T^p = 1$ and $T^c = 999$ leads to poor prediction quality due to the short prediction phase, resulting in a large prediction error and ultimately a failed path. In contrast, (b) uses $T^p = 600$ and $T^c = 400$ which yields a small prediction error and successfully produces a safe and complete path, where the yellow block is being stacked on top of the green block.

Table 6: Maze2D’s training and evaluation hyperparameters

Training	
Loss type	L2
Training steps n_{train}	5.0×10^5
Steps per epoch	2500
Batch size	128
Learning rate	3×10^{-4}
EMA decay	0.995
Evaluation Others	
Planning Horizon H	384
Sampling Horizon T	256
Evaluation SafeFlowMatcher	
Planning Horizon H	384
Prediction Horizon T^p	1
Correction Horizon T^c	256

E.2 PERFORMANCE METRICS

BS quantifies the degree of safety constraint satisfaction using CBFs for each safety constraint in the environment. For each rollout, we evaluate the minimum barrier value over all waypoints, and then take the worst case across all N test episodes:

$$\min_{i=1,2,\dots,N} \min_{k \in \mathcal{H}} b(\tau_1^k).$$

Table 7: Locomotion (Walker2d/Hopper) hyperparameters

Training	
Loss type	L2
Training steps n_{train}	2.5×10^5
Steps per epoch	2500
Batch size	128
Learning rate	2×10^{-4}
EMA decay	0.995
Value Network Training	
Loss type	L2
Training steps n_{train}	5.0×10^4
Steps per epoch	2500
Batch size	128
Learning rate	2×10^{-4}
EMA decay	0.995
Evaluation Others	
Planning Horizon H	600
Sampling Horizon T	20
Evaluation SafeFlowMatcher	
Planning Horizon H	600
Prediction Horizon T^p	1
Correction Horizon T^c	20

Table 8: Robot manipulation (block stacking) hyperparameters

Training	
Loss type	L2
Training steps n_{train}	7.0×10^5
Batch size	64
Learning rate	2×10^{-5}
EMA decay	0.995
Evaluation Others	
Planning Horizon H	128
Sampling Horizon T	1000
Evaluation SafeFlowMatcher	
Planning Horizon H	128
Prediction Horizon T^p	600
Correction Horizon T^c	400

A value $BS \geq 0$ indicates that the path remains entirely within the safe set. Maze2D contains two obstacle-based safety constraints, given by the barrier functions:

$$\mathbf{BS1} : \left(\frac{x - x_0}{a} \right)^2 + \left(\frac{y - y_0}{b} \right)^2 \geq 1, \quad \mathbf{BS2} : \left(\frac{x - x_0}{a} \right)^4 + \left(\frac{y - y_0}{b} \right)^4 \geq 1.$$

where $(x, y) \in \mathbb{R}^2$ denotes the agent's 2D state, $(x_0, y_0) \in \mathbb{R}^2$ specifies the center of the obstacle, and $a, b > 0$ are scaling parameters that shape the corresponding safety region. For locomotion tasks (Walker2D, Hopper), the barrier function is defined as $z \leq h_r$, where $h_r > 0$ denotes the roof height. For robot manipulation (block stacking), the safety constraints enforce joint limits. the barrier functions are defined as $\mathbf{q}_{\min} \leq \mathbf{q} \leq \mathbf{q}_{\max}$, where $\mathbf{q} \in \mathbb{R}^7$ denotes the joint-angle and $\mathbf{q}_{\min}, \mathbf{q}_{\max} \in \mathbb{R}^7$ are the per-joint limits.

1134 **Score** is a normalized, undiscounted performance metric that reflects task success. In Maze2D,
 1135 episodes last up to 800 environment steps while planning is performed over a horizon of $H = 384$;
 1136 once the agent enters a goal neighborhood, it receives a unit reward for each remaining step, making
 1137 the score proportional to the remaining horizon. For locomotion tasks, the score is proportional
 1138 to forward displacement and normalized such that reaching the target position $x = 1$ yields a score
 1139 of 1. We evaluate locomotion in a receding-horizon manner, continuing until the agent either reaches
 1140 $x = 1$, falls, or reaches the maximum episode limit of 1000 steps. For a robot manipulation (block
 1141 stacking), planning is performed with horizon $H = 128$, and each episode attempts a single stacking
 1142 action. An episode receives a score of 1 upon a successful stack and 0 otherwise.

1143 **Trap Rate** measures the rate of local traps, i.e., the percentage of episodes in which the generated
 1144 path becomes stuck against barrier constraints; see Definition 2.

1145 **T-Time & S-Time.** We report two timing metrics: the total computation time (T-Time) and the per-
 1146 step sampling time (S-Time), both of which include all computational overheads such as CBF-QP
 1147 evaluations. T-Time measures the total wall-clock time required to generate an entire path, including
 1148 all prediction and correction steps when applicable. S-Time reports the average wall-clock time per
 1149 sampling step, computed as S-Time = T-Time/ T , where T is the total sampling horizon.

1150 **Curvature (κ)** measures local path bending using the Menger curvature computed from triplets of
 1151 consecutive points. We report the average curvature along the path.

1153 **Acceleration (α)** captures the change in velocity across consecutive time steps. It is computed as
 1154 the mean squared acceleration magnitude along the path. We approximate it via the second-order
 1155 finite difference of the 2D position and define the metric as the average acceleration magnitude
 1156 along the path.

1158 F ADDITIONAL ABLATION STUDIES

1160 F.1 HANDLING MULTIPLE CBF CONSTRAINTS AND MITIGATING COMPUTATION 1161 BOTTLENECK

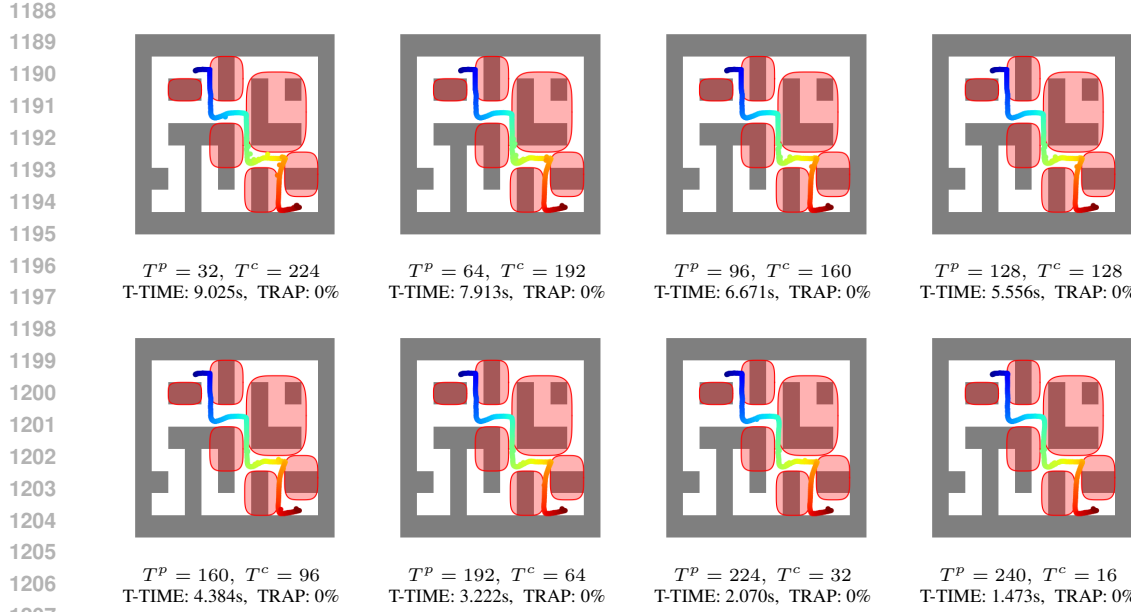
1163 We considered only two CBF constraints so far. When more than two constraints are present, no
 1164 closed-form solution is available, and a QP solver must be used to compute the CBF-QP at every
 1165 step. This inevitably increases computational overhead and can become a bottleneck.

1166 Figure 13 presents the path generation results with six CBF constraints, under a fixed sampling
 1167 horizon $T = 256$, while varying the allocation between prediction and correction horizon (T^p, T^c).
 1168 The corresponding T-TIME and Trap Rate for each configuration are also reported. We observe
 1169 that SafeFlowMatcher maintains a trap rate of 0% across all settings. However, as T^c increases, the
 1170 T-TIME grows due to repeated CBF-QP solves during the correction phase.

1171 A key advantage of SafeFlowMatcher is that the PC integrator naturally mitigates this computational
 1172 bottleneck. Since CBF-QP computations occur only in the correction phase, T^p and T^c can be
 1173 adjusted to reduce the number of QP evaluations while maintaining safety. In contrast, SafeDiffuser
 1174 and SafeFM require CBF-QP computations at every generation step, resulting in significantly higher
 1175 overhead when many constraints are present. Moreover, SafeDiffuser becomes unstable in high-
 1176 constraint settings. As presented in Table 1, local traps are already problematic in the two constraints
 1177 setting, they occur even more frequently as the number of safety constraints increases. In the six CBF
 1178 constraints setting, SafeDiffuser required T-TIME = 10.269 s and exhibited a 100% trap rate over
 1179 100 runs. These observations highlight that the PC integrator enables SafeFlowMatcher to scale
 1180 efficiently and robustly to environments with many CBF constraints, both in terms of computational
 1181 latency and safe path generation.

1183 F.2 EXPLORING THE FEASIBLE RANGE OF CBF HYPERPARAMETERS ρ AND ϵ

1185 We examine the sensitivity of SafeFlowMatcher and SafeFM to the CBF hyperparameters ρ and ϵ .
 1186 Smaller ρ or larger ϵ induce more aggressive safety corrections, which can help fast convergence to
 1187 a safe set but may also increase curvature. When excessively strong, these corrections can even lead
 1188 to unstable or oscillatory behavior.



1208 **Figure 13: Balancing prediction and correction horizon in narrow-corridor setting.** Visualization
1209 of the prediction–correction trade-off under a fixed total sampling horizon $T = T^p + T^c = 256$.
1210 Each result shows the resulting path for a different allocation of prediction steps T^p and correction
1211 steps T^c in the narrow-corridor setting.

1212
1213
1214 Across a sweep of $\rho \in \{0.1, 0.3, 0.5, 0.7, 0.9\}$ and $\epsilon \in \{0.25, 0.50, 1.00, 2.50, 5.00, 10.00\}$, Safe-
1215 FlowMatcher which include PC integrator remains stable over a significantly broader hyperparameter
1216 range than SafeFM (the correction-only variant), making it substantially easier to tune in practice.
1217 This behavior is consistent with Remark 1, which explains that the prediction phase places the path
1218 closer to a region where safety enforcement is feasible and well-conditioned, resulting in more ro-
1219 bust behavior under different CBF strengths.
1220

1221 **Table 9: Comparison between SafeFlowMatcher and SafeFM on CBF hyperparameters.** Sub-
1222 set of the (ρ, ϵ) hyperparameter grid in Maze2D, comparing SafeFlowMatcher (ours) and SafeFM
1223 (w/o PC). Each entry reports mean \pm std over 100 rollouts for Score, Trap Rate, curvature (κ), ac-
1224 celeration (a), and minimum barrier values (BS1, BS2).

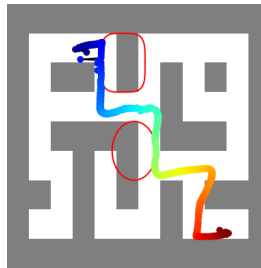
ρ	ϵ	Score		Trap Rate		$\kappa \downarrow$		$a \downarrow$		BS1		BS2	
		Ours	w/o PC	Ours	w/o PC	Ours	w/o PC	Ours	w/o PC	Ours	w/o PC	Ours	w/o PC
0.1	0.25	1.632 \pm 0.003	0.446 \pm 0.649	0%	100%	76.640 \pm 1.446	1.766 \pm 0.209	94.579 \pm 1.116	2.180e+04 \pm 1.083e+04	0.010	-0.058	0.009	-0.101
0.1	0.50	1.633 \pm 0.003	0.526 \pm 0.673	0%	100%	77.919 \pm 1.570	1.961 \pm 0.257	96.953 \pm 1.408	2.713e+04 \pm 4.833e+04	0.010	-0.189	0.009	-0.211
0.1	1.00	1.632 \pm 0.003	0.639 \pm 0.691	0%	100%	78.349 \pm 1.561	2.275 \pm 0.317	102.139 \pm 3.267	2.536e+04 \pm 4.340e+04	0.010	-0.041	0.010	-0.200
0.1	2.50	1.633 \pm 0.003	0.709 \pm 0.699	0%	100%	79.337 \pm 1.898	3.041 \pm 0.413	109.303 \pm 6.840	1.755e+04 \pm 1.035e+04	0.010	-0.022	0.010	-0.383
0.1	5.00	1.633 \pm 0.004	1.025 \pm 0.613	5%	100%	80.416 \pm 1.605	3.871 \pm 0.556	141.126 \pm 16.164	4.188e+04 \pm 2.735e+04	0.010	-0.111	0.009	-0.107
0.1	10.00	1.633 \pm 0.005	1.323 \pm 0.438	50%	100%	81.395 \pm 1.435	5.147 \pm 0.581	174.368 \pm 31.192	1.160e+04 \pm 2.497e+04	0.010	-0.888	0.010	-0.111
0.3	0.25	1.632 \pm 0.003	0.628 \pm 0.685	0%	100%	73.121 \pm 1.286	2.205 \pm 0.334	92.501 \pm 0.775	1.885e+04 \pm 4.554e+03	0.010	-0.036	0.008	0.014
0.3	0.50	1.632 \pm 0.004	0.702 \pm 0.727	0%	100%	75.438 \pm 1.267	2.765 \pm 0.386	93.140 \pm 0.740	1.895e+04 \pm 1.503e+04	0.010	-0.056	0.009	0.017
0.3	1.00	1.632 \pm 0.003	0.812 \pm 0.669	0%	100%	77.971 \pm 1.377	4.105 \pm 0.561	93.835 \pm 0.949	4.505e+04 \pm 1.266e+05	0.010	-0.050	0.009	0.021
0.3	2.50	1.634 \pm 0.003	1.136 \pm 0.588	0%	100%	78.486 \pm 1.510	7.826 \pm 1.811	95.123 \pm 1.614	1.333e+04 \pm 3.713e+04	0.010	-0.045	0.009	0.029
0.3	5.00	1.633 \pm 0.003	1.323 \pm 0.503	0%	100%	79.055 \pm 1.453	15.566 \pm 3.422	101.603 \pm 3.888	3.710e+04 \pm 8.006e+02	0.010	-0.122	0.009	0.067
0.3	10.00	1.633 \pm 0.003	1.323 \pm 0.438	0%	100%	79.345 \pm 1.786	21.111 \pm 4.519	113.198 \pm 8.455	3.093e+03 \pm 1.456e+03	0.010	-0.240	0.010	0.071
0.5	0.25	1.632 \pm 0.003	1.083 \pm 0.581	0%	100%	70.276 \pm 1.101	4.186 \pm 0.607	92.016 \pm 0.787	1.953e+04 \pm 3.482e+04	0.009	-0.005	0.008	-0.005
0.5	0.50	1.631 \pm 0.007	1.318 \pm 0.481	0%	100%	72.149 \pm 1.218	8.378 \pm 1.172	92.333 \pm 0.676	4.498e+04 \pm 2.718e+05	0.010	-0.044	0.008	-0.047
0.5	1.00	1.632 \pm 0.005	1.356 \pm 0.418	0%	100%	74.715 \pm 1.251	10.205 \pm 4.803	92.021 \pm 0.760	5.606e+04 \pm 1.862e+04	0.010	-0.190	0.009	-0.181
0.5	2.50	1.632 \pm 0.004	1.404 \pm 0.363	0%	94%	77.717 \pm 1.436	62.906 \pm 16.457	91.634 \pm 0.676	1.370e+03 \pm 5.066e+03	0.010	-0.550	0.009	-0.623
0.5	5.00	1.633 \pm 0.003	1.424 \pm 0.419	0%	100%	78.220 \pm 1.389	48.093 \pm 6.626	92.980 \pm 1.315	1.015e+03 \pm 2.653e+02	0.010	-0.529	0.010	-0.813
0.5	10.00	1.632 \pm 0.009	1.334 \pm 0.474	0%	100%	78.742 \pm 1.554	31.623 \pm 4.874	96.749 \pm 2.255	2.011e+03 \pm 1.126e+03	0.010	-0.478	0.010	-0.634
0.7	0.25	1.632 \pm 0.005	1.416 \pm 0.423	0%	97%	69.277 \pm 1.121	46.769 \pm 16.247	92.030 \pm 0.821	3.148e+03 \pm 9.812e+03	0.010	0.075	-0.039	0.004
0.7	0.50	1.632 \pm 0.003	1.318 \pm 0.511	0%	29%	70.150 \pm 1.057	63.292 \pm 20.617	92.006 \pm 0.832	4.445e+03 \pm 2.939e+03	0.009	0.129	0.008	-0.002
0.7	1.00	1.632 \pm 0.003	1.38 \pm 0.453	0%	49%	71.967 \pm 1.215	70.206 \pm 21.172	91.808 \pm 0.642	1.733e+04 \pm 1.123e+05	0.010	0.042	0.008	-0.083
0.7	2.50	1.632 \pm 0.004	1.389 \pm 0.450	0%	90%	74.581 \pm 1.317	69.241 \pm 15.931	90.505 \pm 0.637	4.953e+04 \pm 4.876e+05	0.010	-0.037	0.008	-0.552
0.7	5.00	1.633 \pm 0.003	1.277 \pm 0.525	0%	100%	76.222 \pm 1.362	52.326 \pm 9.061	90.312 \pm 0.615	9.065e+02 \pm 3.554e+02	0.010	-0.064	0.009	-0.767
0.7	10.00	1.632 \pm 0.007	1.363 \pm 0.394	0%	100%	77.335 \pm 1.329	35.424 \pm 5.417	91.406 \pm 0.738	1.606e+03 \pm 3.131e+02	0.010	-0.094	0.009	-0.716
0.9	0.25	1.631 \pm 0.011	1.321 \pm 0.526	0%	17%	71.163 \pm 1.132	59.639 \pm 20.682	91.879 \pm 0.629	1.688e+04 \pm 1.575e+05	-0.010	-0.055	-0.101	-0.047
0.9	0.50	1.632 \pm 0.004	1.421 \pm 0.380	0%	25%	69.218 \pm 0.897	58.677 \pm 20.838	92.114 \pm 0.786	1.040e+03 \pm 3.773e+03	0.010	0.010	0.010	0.011
0.9	1.00	1.632 \pm 0.006	1.335 \pm 0.473	0%	26%	70.471 \pm 0.955	63.532 \pm 21.366	91.757 \pm 0.777	4.596e+03 \pm 3.320e+04	0.010	0.002	0.010	-0.011
0.9	2.50	1.632 \pm 0.003	1.406 \pm 0.428	0%	79%	72.022 \pm 1.198	70.335 \pm 17.711	90.333 \pm 0.703	43.667 \pm 572.690	0.010	-0.514	0.008	-0.553
0.9	5.00	1.633 \pm 0.003	1.391 \pm 0.410	0%	100%	72.987 \pm 1.284	57.745 \pm 10.115	89.935 \pm 0.688	743.566 \pm 262.536	0.010	-0.530	0.008	-0.691
0.9	10.00	1.632 \pm 0.003	1.419 \pm 0.361	0%	100%	74.981 \pm 1.450	40.196 \pm 5.018	89.995 \pm 0.664	1.350e+03 \pm 255.700	0.010	-0.434	0.009	-0.759

1242 F.3 EFFICIENCY OF SAFEFLOWMATCHER ACROSS CORRECTION HORIZONS
12431244 Table 10: **Closed-Form CBF Solver: Computation time across correction horizons.** Comparison
1245 of RES-SafeDiffuser with a fixed sampling horizon $T = 256$ and SafeFlowMatcher for a fixed pre-
1246 diction horizon $T^p = 1$ and varying correction horizons $T^c \in \{4, 8, 16, 32, 64, 128, 256\}$ in Maze2D,
1247 when using the closed-form solution of CBF-QP. Each entry reports mean \pm std over 100 rollouts.
1248

Method (Closed-Form CBF)	Score (\uparrow)	T-Time (s)	Trap Rate	$\kappa(\downarrow)$	$a(\downarrow)$	BS1&BS2 (≥ 0)
RES-SafeDiffuser (Xiao et al., 2025)	1.442 \pm 0.451	1.208	72%	80.30 \pm 13.06	398.17 \pm 1060.86	Yes
SafeFlowMatcher ($T^c=4$)	1.610 \pm 0.029	0.023	17%	79.26 \pm 2.29	252.01 \pm 18.19	Yes
SafeFlowMatcher ($T^c=8$)	1.627 \pm 0.018	0.042	0%	75.72 \pm 1.64	114.03 \pm 6.33	Yes
SafeFlowMatcher ($T^c=16$)	1.634 \pm 0.002	0.078	0%	67.96 \pm 1.11	89.29 \pm 0.96	Yes
SafeFlowMatcher ($T^c=32$)	1.634 \pm 0.003	0.155	0%	67.48 \pm 1.09	87.33 \pm 0.85	Yes
SafeFlowMatcher ($T^c=64$)	1.633 \pm 0.003	0.299	0%	68.03 \pm 1.01	89.09 \pm 0.73	Yes
SafeFlowMatcher ($T^c=128$)	1.632 \pm 0.003	0.617	0%	69.72 \pm 0.98	91.01 \pm 0.90	Yes
SafeFlowMatcher ($T^c=256$)	1.632 \pm 0.003	1.215	0%	69.19 \pm 1.02	91.90 \pm 0.77	Yes

1255
1256
1257 Table 11: **QP-Based CBF Solver: Computation time across correction horizons.** Comparison of
1258 RES-SafeDiffuser with a fixed sampling horizon $T = 256$ and SafeFlowMatcher for a fixed prediction
1259 horizon $T^p = 1$ and varying correction horizons $T^c \in \{4, 8, 16, 32, 64, 128, 256\}$ in Maze2D,
1260 when using the QP solver solution of CBF-QP. Each entry reports mean \pm std over 100 rollouts.
1261

Method (QP CBF Solver)	Score (\uparrow)	T-Time (s)	Trap Rate	$\kappa(\downarrow)$	$a(\downarrow)$	BS1&BS2 (≥ 0)
RES-SafeDiffuser (Xiao et al., 2025)	1.468 \pm 0.353	9.998	85%	76.06 \pm 38.73	4776.45 \pm 2430.48	Yes
SafeFlowMatcher ($T^c=4$)	1.606 \pm 0.029	0.157	12%	77.31 \pm 2.52	276.02 \pm 39.01	Yes
SafeFlowMatcher ($T^c=8$)	1.632 \pm 0.004	0.315	4%	76.93 \pm 1.11	137.31 \pm 11.00	Yes
SafeFlowMatcher ($T^c=16$)	1.634 \pm 0.003	0.613	0%	67.94 \pm 1.31	118.72 \pm 9.65	Yes
SafeFlowMatcher ($T^c=32$)	1.632 \pm 0.007	1.247	0%	68.54 \pm 1.22	154.20 \pm 14.70	Yes
SafeFlowMatcher ($T^c=64$)	1.632 \pm 0.003	2.464	2%	69.54 \pm 1.44	158.70 \pm 23.97	Yes
SafeFlowMatcher ($T^c=128$)	1.631 \pm 0.004	4.892	11%	70.59 \pm 1.46	174.57 \pm 34.67	Yes
SafeFlowMatcher ($T^c=256$)	1.630 \pm 0.004	9.957	13%	67.80 \pm 1.42	183.47 \pm 28.39	Yes

1262
1263
1264
1265
1266
1267
1268
1269
1270 Across both the closed-form and QP-based CBF solvers, SafeFlowMatcher exhibits exceptionally
1271 low generation time (T-Time), even when the correction horizon is small. The tables show that Safe-
1272 FlowMatcher remains effective and safe over a wide range of T^c values, whereas RES-SafeDiffuser
1273 is much slower and frequently suffers from severe local traps. At $T^c = 4$, SafeFlowMatcher may
1274 exhibit minor oscillations near constraint boundaries due to overcorrections caused by the small
1275 correction steps (see Figure 14). Although this falls under the definition of the local trap in 2, its impact
1276 is minimal, in contrast to SafeDiffuser, whose early safety enforcement often leads to hard traps and
1277 incomplete paths (see Figure 16).1278 Figure 14: **Local trap of SafeFlowMatcher at $T^c = 4$.** Local traps observed at small correction
1279 horizons $T^c = 4$ in Maze2D. These traps manifest as mild boundary oscillations near obstacles, yet
1280 the path remains complete and reaches the goal. Unlike SafeDiffuser depicted in Figure 16, which
1281 often fails with incomplete paths under early safety enforcement, SafeFlowMatcher maintains path
1282 completeness despite minor oscillations.
1283
1284
1285
12861287
1288
1289
1290
1291
1292
1293
1294
1295

1296 F.4 ENERGY-DISTANCE ANALYSIS OF DISTRIBUTIONAL DRIFT INDUCED BY CONTROL
 1297 BARRIER FUNCTIONS
 1298

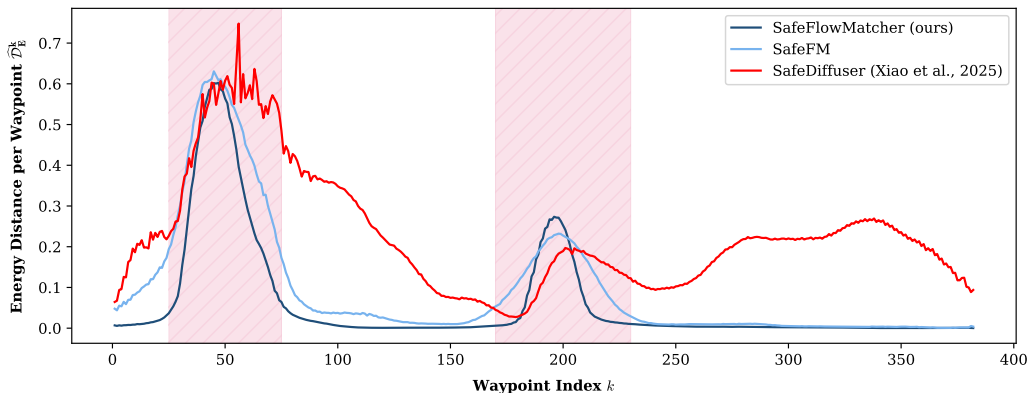
1299 We quantify how much each perturbation $\Delta \mathbf{u}_t^k$ affects the generative process by measuring an energy
 1300 distance between paths with and without safety intervention. For each model pair (FlowMatcher
 1301 vs. SafeFlowMatcher, FM vs. SafeFM, Diffuser (Janner et al., 2022) vs. SafeDiffuser (Xiao et al.,
 1302 2025)), we generate $N = 100$ paths from both the baseline and the corresponding safe variants,
 1303 starting from the same initial conditions. We define the distance between two paths as the average
 1304 waypoint-wise Euclidean distance

$$1305 \delta(\boldsymbol{\tau}, \boldsymbol{\tau}') = \frac{1}{H+1} \sum_{k=0}^H \|\boldsymbol{\tau}^k - \boldsymbol{\tau}'^k\|_2.$$

1306 Given $\{\boldsymbol{\tau}_{1,i}^{\text{base}}\}_{i=1}^N$ and $\{\boldsymbol{\tau}_{1,j}^{\text{safe}}\}_{j=1}^N$, where $\boldsymbol{\tau}_{1,(\cdot)}$ denotes the final generated path⁶, the (sample) energy
 1307 distance between the two path distributions is

$$1308 \widehat{\mathcal{D}}_E = \frac{2}{N^2} \sum_{i=1}^N \sum_{j=1}^N \delta(\boldsymbol{\tau}_{1,i}^{\text{base}}, \boldsymbol{\tau}_{1,j}^{\text{safe}}) - \frac{1}{N^2} \sum_{i=1}^N \sum_{j=1}^N \delta(\boldsymbol{\tau}_{1,i}^{\text{base}}, \boldsymbol{\tau}_{1,j}^{\text{base}}) - \frac{1}{N^2} \sum_{i=1}^N \sum_{j=1}^N \delta(\boldsymbol{\tau}_{1,i}^{\text{safe}}, \boldsymbol{\tau}_{1,j}^{\text{safe}}).$$

1310 Larger values indicate stronger distributional drift between the baseline and safe path distributions.
 1311 For each waypoint k , we similarly define a per-waypoint energy distance $\widehat{\mathcal{D}}_E^k$ by replacing $\delta(\boldsymbol{\tau}, \boldsymbol{\tau}')$
 1312 with $\delta^k(\boldsymbol{\tau}, \boldsymbol{\tau}') = \|\boldsymbol{\tau}^k - \boldsymbol{\tau}'^k\|_2$ in the above definition of $\widehat{\mathcal{D}}_E$.
 1313



1314 Figure 15: **Per-waypoint drift between baseline and safe path.** For each model pair (Flow-
 1315 Matcher/SafeFlowMatcher, FM/SafeFM, Diffuser/SafeDiffuser), the plot shows the mean per-
 1316 waypoint deviation between paths produced by the baseline and its corresponding safe variant. The
 1317 pink band marks the region where the baseline path violates the CBF constraint at the final time; for
 1318 clarity, a single common band is shown, although the exact violation interval may differ by several
 1319 steps across models.

1320
 1321
 1322
 1323
 1324
 1325
 1326
 1327
 1328
 1329
 1330
 1331 Figure 15 plots the per-waypoint energy distance $\widehat{\mathcal{D}}_E^k$ between the baseline and safe paths. Across the
 1332 three model pairs, the resulting energy distances $\widehat{\mathcal{D}}_E$ are 0.061 (SafeFlowMatcher), 0.097 (SafeFM),
 1333 and 0.229 (SafeDiffuser), showing that SafeFlowMatcher induces the smallest distributional drift
 1334 while still enforcing safety. The pink band indicates the segment in which the baseline path violates
 1335 the CBF constraint at the final time. Outside this safety-critical region, SafeDiffuser shows large
 1336 drift, and SafeFM still exhibits noticeable spillover, suggesting that their safety interventions propa-
 1337 gate to parts of the path that do not require correction. In contrast, SafeFlowMatcher keeps the drift
 1338 close to zero outside the pink band.

1339 In SafeFM and SafeDiffuser, the perturbation is applied not only at $t = 1$, but also to intermediate
 1340 generative states $\boldsymbol{\tau}_t^k$ for $t \in [0, 1]$ that are never executed. Once these perturbed intermediate states

1341
 1342
 1343
 1344
 1345
 1346
 1347
 1348
 1349
 1350
 1351
 1352
 1353
 1354
 1355
 1356
 1357
 1358
 1359
 1360
 1361
 1362
 1363
 1364
 1365
 1366
 1367
 1368
 1369
 1370
 1371
 1372
 1373
 1374
 1375
 1376
 1377
 1378
 1379
 1380
 1381
 1382
 1383
 1384
 1385
 1386
 1387
 1388
 1389
 1390
 1391
 1392
 1393
 1394
 1395
 1396
 1397
 1398
 1399
 1400
 1401
 1402
 1403
 1404
 1405
 1406
 1407
 1408
 1409
 1410
 1411
 1412
 1413
 1414
 1415
 1416
 1417
 1418
 1419
 1420
 1421
 1422
 1423
 1424
 1425
 1426
 1427
 1428
 1429
 1430
 1431
 1432
 1433
 1434
 1435
 1436
 1437
 1438
 1439
 1440
 1441
 1442
 1443
 1444
 1445
 1446
 1447
 1448
 1449
 1450
 1451
 1452
 1453
 1454
 1455
 1456
 1457
 1458
 1459
 1460
 1461
 1462
 1463
 1464
 1465
 1466
 1467
 1468
 1469
 1470
 1471
 1472
 1473
 1474
 1475
 1476
 1477
 1478
 1479
 1480
 1481
 1482
 1483
 1484
 1485
 1486
 1487
 1488
 1489
 1490
 1491
 1492
 1493
 1494
 1495
 1496
 1497
 1498
 1499
 1500
 1501
 1502
 1503
 1504
 1505
 1506
 1507
 1508
 1509
 1510
 1511
 1512
 1513
 1514
 1515
 1516
 1517
 1518
 1519
 1520
 1521
 1522
 1523
 1524
 1525
 1526
 1527
 1528
 1529
 1530
 1531
 1532
 1533
 1534
 1535
 1536
 1537
 1538
 1539
 1540
 1541
 1542
 1543
 1544
 1545
 1546
 1547
 1548
 1549
 1550
 1551
 1552
 1553
 1554
 1555
 1556
 1557
 1558
 1559
 1560
 1561
 1562
 1563
 1564
 1565
 1566
 1567
 1568
 1569
 1570
 1571
 1572
 1573
 1574
 1575
 1576
 1577
 1578
 1579
 1580
 1581
 1582
 1583
 1584
 1585
 1586
 1587
 1588
 1589
 1590
 1591
 1592
 1593
 1594
 1595
 1596
 1597
 1598
 1599
 1600
 1601
 1602
 1603
 1604
 1605
 1606
 1607
 1608
 1609
 1610
 1611
 1612
 1613
 1614
 1615
 1616
 1617
 1618
 1619
 1620
 1621
 1622
 1623
 1624
 1625
 1626
 1627
 1628
 1629
 1630
 1631
 1632
 1633
 1634
 1635
 1636
 1637
 1638
 1639
 1640
 1641
 1642
 1643
 1644
 1645
 1646
 1647
 1648
 1649
 1650
 1651
 1652
 1653
 1654
 1655
 1656
 1657
 1658
 1659
 1660
 1661
 1662
 1663
 1664
 1665
 1666
 1667
 1668
 1669
 1670
 1671
 1672
 1673
 1674
 1675
 1676
 1677
 1678
 1679
 1680
 1681
 1682
 1683
 1684
 1685
 1686
 1687
 1688
 1689
 1690
 1691
 1692
 1693
 1694
 1695
 1696
 1697
 1698
 1699
 1700
 1701
 1702
 1703
 1704
 1705
 1706
 1707
 1708
 1709
 1710
 1711
 1712
 1713
 1714
 1715
 1716
 1717
 1718
 1719
 1720
 1721
 1722
 1723
 1724
 1725
 1726
 1727
 1728
 1729
 1730
 1731
 1732
 1733
 1734
 1735
 1736
 1737
 1738
 1739
 1740
 1741
 1742
 1743
 1744
 1745
 1746
 1747
 1748
 1749
 1750
 1751
 1752
 1753
 1754
 1755
 1756
 1757
 1758
 1759
 1760
 1761
 1762
 1763
 1764
 1765
 1766
 1767
 1768
 1769
 1770
 1771
 1772
 1773
 1774
 1775
 1776
 1777
 1778
 1779
 1780
 1781
 1782
 1783
 1784
 1785
 1786
 1787
 1788
 1789
 1790
 1791
 1792
 1793
 1794
 1795
 1796
 1797
 1798
 1799
 1800
 1801
 1802
 1803
 1804
 1805
 1806
 1807
 1808
 1809
 1810
 1811
 1812
 1813
 1814
 1815
 1816
 1817
 1818
 1819
 1820
 1821
 1822
 1823
 1824
 1825
 1826
 1827
 1828
 1829
 1830
 1831
 1832
 1833
 1834
 1835
 1836
 1837
 1838
 1839
 1840
 1841
 1842
 1843
 1844
 1845
 1846
 1847
 1848
 1849
 1850
 1851
 1852
 1853
 1854
 1855
 1856
 1857
 1858
 1859
 1860
 1861
 1862
 1863
 1864
 1865
 1866
 1867
 1868
 1869
 1870
 1871
 1872
 1873
 1874
 1875
 1876
 1877
 1878
 1879
 1880
 1881
 1882
 1883
 1884
 1885
 1886
 1887
 1888
 1889
 1890
 1891
 1892
 1893
 1894
 1895
 1896
 1897
 1898
 1899
 1900
 1901
 1902
 1903
 1904
 1905
 1906
 1907
 1908
 1909
 1910
 1911
 1912
 1913
 1914
 1915
 1916
 1917
 1918
 1919
 1920
 1921
 1922
 1923
 1924
 1925
 1926
 1927
 1928
 1929
 1930
 1931
 1932
 1933
 1934
 1935
 1936
 1937
 1938
 1939
 1940
 1941
 1942
 1943
 1944
 1945
 1946
 1947
 1948
 1949
 1950
 1951
 1952
 1953
 1954
 1955
 1956
 1957
 1958
 1959
 1960
 1961
 1962
 1963
 1964
 1965
 1966
 1967
 1968
 1969
 1970
 1971
 1972
 1973
 1974
 1975
 1976
 1977
 1978
 1979
 1980
 1981
 1982
 1983
 1984
 1985
 1986
 1987
 1988
 1989
 1990
 1991
 1992
 1993
 1994
 1995
 1996
 1997
 1998
 1999
 2000
 2001
 2002
 2003
 2004
 2005
 2006
 2007
 2008
 2009
 2010
 2011
 2012
 2013
 2014
 2015
 2016
 2017
 2018
 2019
 2020
 2021
 2022
 2023
 2024
 2025
 2026
 2027
 2028
 2029
 2030
 2031
 2032
 2033
 2034
 2035
 2036
 2037
 2038
 2039
 2040
 2041
 2042
 2043
 2044
 2045
 2046
 2047
 2048
 2049
 2050
 2051
 2052
 2053
 2054
 2055
 2056
 2057
 2058
 2059
 2060
 2061
 2062
 2063
 2064
 2065
 2066
 2067
 2068
 2069
 2070
 2071
 2072
 2073
 2074
 2075
 2076
 2077
 2078
 2079
 2080
 2081
 2082
 2083
 2084
 2085
 2086
 2087
 2088
 2089
 2090
 2091
 2092
 2093
 2094
 2095
 2096
 2097
 2098
 2099
 2100
 2101
 2102
 2103
 2104
 2105
 2106
 2107
 2108
 2109
 2110
 2111
 2112
 2113
 2114
 2115
 2116
 2117
 2118
 2119
 2120
 2121
 2122
 2123
 2124
 2125
 2126
 2127
 2128
 2129
 2130
 2131
 2132
 2133
 2134
 2135
 2136
 2137
 2138
 2139
 2140
 2141
 2142
 2143
 2144
 2145
 2146
 2147
 2148
 2149
 2150
 2151
 2152
 2153
 2154
 2155
 2156
 2157
 2158
 2159
 2160
 2161
 2162
 2163
 2164
 2165
 2166
 2167
 2168
 2169
 2170
 2171
 2172
 2173
 2174
 2175
 2176
 2177
 2178
 2179
 2180
 2181
 2182
 2183
 2184
 2185
 2186
 2187
 2188
 2189
 2190
 2191
 2192
 2193
 2194
 2195
 2196
 2197
 2198
 2199
 2200
 2201
 2202
 2203
 2204
 2205
 2206
 2207
 2208
 2209
 2210
 2211
 2212
 2213
 2214
 2215
 2216
 2217
 2218
 2219
 2220
 2221
 2222
 2223
 2224
 2225
 2226
 2227
 2228
 2229
 2230
 2231
 2232
 2233
 2234
 2235
 2236
 2237
 2238
 2239
 2240
 2241
 2242
 2243
 2244
 2245
 2246
 2247
 2248
 2249
 2250
 2251
 2252
 2253
 2254
 2255
 2256
 2257
 2258
 2259
 2260
 2261
 2262
 2263
 2264
 2265
 2266
 2267
 2268
 2269
 2270
 2271
 2272
 2273
 2274
 2275
 2276
 2277
 2278
 2279
 2280
 2281
 2282
 2283
 2284
 2285
 2286
 2287
 2288
 2289
 2290
 2291
 2292
 2293
 2294
 2295
 2296
 2297
 2298
 2299
 2300
 2301
 2302
 2303
 2304
 2305
 2306
 2307
 2308
 2309
 2310
 2311
 2312
 2313
 2314
 2315
 2316
 2317
 2318
 2319
 2320
 2321
 2322
 2323
 2324
 2325
 2326
 2327
 2328
 2329
 2330
 2331
 2332
 2333
 2334
 2335
 2336
 2337
 2338
 2339
 2340
 2341
 2342
 2343
 2344
 2345
 2346
 2347
 2348
 2349
 2350
 2351
 2352
 2353
 2354
 2355
 2356
 2357
 2358
 2359
 2360
 2361
 2362
 2363
 2364
 2365
 2366
 2367
 2368
 2369
 2370
 2371
 2372
 2373
 2374
 2375
 2376
 2377
 2378
 2379
 2380
 2381
 2382
 2383
 2384
 2385
 2386
 2387
 2388
 2389
 2390
 2391
 2392
 2393
 2394
 2395
 2396
 2397
 2398
 2399
 2400
 2401
 2402
 2403
 2404
 2405
 2406
 2407
 2408
 2409
 2410
 2411
 2412
 2413
 2414
 2415
 2416
 2417
 2418
 2419
 2420
 2421
 2422
 2423
 2424
 2425
 2426
 2427
 2428
 2429
 2430
 2431
 2432
 2433
 2434
 2435
 2436
 2437
 2438
 2439
 2440
 2441
 2442
 2443
 2444
 2445
 2446
 2447
 2448
 2449
 2450
 2451
 2452
 2453
 2454
 2455
 2456
 2457
 2458
 2459
 2460
 2461
 2462
 2463
 2464
 2465
 2466
 2467
 2468
 2469
 2470
 2471
 2472
 2473
 2474
 2475
 2476
 2477
 2478
 2479
 2480
 2481
 2482
 2483
 2484
 2485
 2486
 2487
 2488
 2489
 2490
 2491
 2492
 2493
 2494
 2495
 2496
 2497
 2498
 2499
 2500
 2501
 2502
 2503
 2504
 2505
 2506
 2507
 2508
 2509
 2510
 2511
 2512
 2513
 2514
 2515
 2516
 2517<br

1350
 1351 are fed back into the velocity field and integrated forward, the resulting deviations can accumulate
 1352 and propagate through the generative dynamics, producing drift at waypoints far outside the final-
 1353 time violation interval. However, PC integrator in SafeFlowMatcher naturally separate correction
 1354 from the prediction. It can mitigate this kind of drift effectively.
 1355

1356 F.5 VISUALIZATION AND QUALITATIVE ANALYSIS OF LOCAL TRAPS

1357 Following the Definition 2, a path is locally trapped if the corrected waypoint exhibits a large dis-
 1358 continuity between two successive corrected path:
 1359

$$\|\tau_1^k - \tau_1^{k-1}\| > \zeta,$$

1361 for some threshold $\zeta > 0$. Intuitively, this corresponds to path that get stuck near safety boundaries
 1362 and consequently produce a large *jump* to escape, often resulting in incomplete paths.
 1363

1364 **SafeDiffuser** applies the CBF constraint to each waypoint at every sampling step, starting from pure
 1365 noise. Because the initial waypoints are sampled i.i.d., neighboring waypoints τ_t^k and τ_t^{k-1} often
 1366 differ significantly. Since CBFs depend on the state, such large discrepancies cause the resulting CBF
 1367 corrections to vary greatly across waypoints. Although the diffuser aims to generate a continuous
 1368 path (i.e., $\|\tau_t^k - \tau_t^{k-1}\| \leq \zeta$), applying the CBF constraint independently at each waypoint can break
 1369 this continuity, pushing different waypoints toward different constraint boundaries and creating local
 1370 traps. This behavior is clearly visualized in Figures 16 and 17.

1371 **SafeFlowMatcher**, in contrast, begins the correction phase from a semi-continuous path τ_0^c (i.e.,
 1372 $\|\tau_0^{c,k} - \tau_0^{c,k-1}\| \leq \eta$ for some small $\eta \geq \zeta$). Because neighboring waypoints are already close to
 1373 each other, the resulting CBF corrections vary smoothly across the path. This keeps all waypoints
 1374 moving in a consistent direction, preserving the path’s continuity and preventing local traps. As
 1375 visualized in Figures 18 and 19, the path maintains forward progress without stalling.
 1376

1377
 1378
 1379
 1380
 1381
 1382
 1383
 1384
 1385
 1386
 1387
 1388
 1389
 1390
 1391
 1392
 1393
 1394
 1395
 1396
 1397
 1398
 1399
 1400
 1401
 1402
 1403



1446 **Figure 16: Path Generation Process of SafeDiffuser (Xiao et al., 2025) in Maze2D environment**
 1447 **with two constraints.** From the top-left to the bottom-right, we visualize τ_t on a uniform time
 1448 discretization of $[T, 0]$, excluding the midpoint $t = 0.5T$.

1449
 1450
 1451
 1452
 1453
 1454
 1455
 1456
 1457

1458

1459

1460

1461

1462

1463

1464

1465

1466

1467

1468

1469

1470

1471

1472

1473

1474

1475

1476

1477

1478

1479

1480

1481

1482

1483

1484

1485

1486

1487

1488

1489

1490

1491

1492

1493

1494

1495

1496

1497

1498

1499

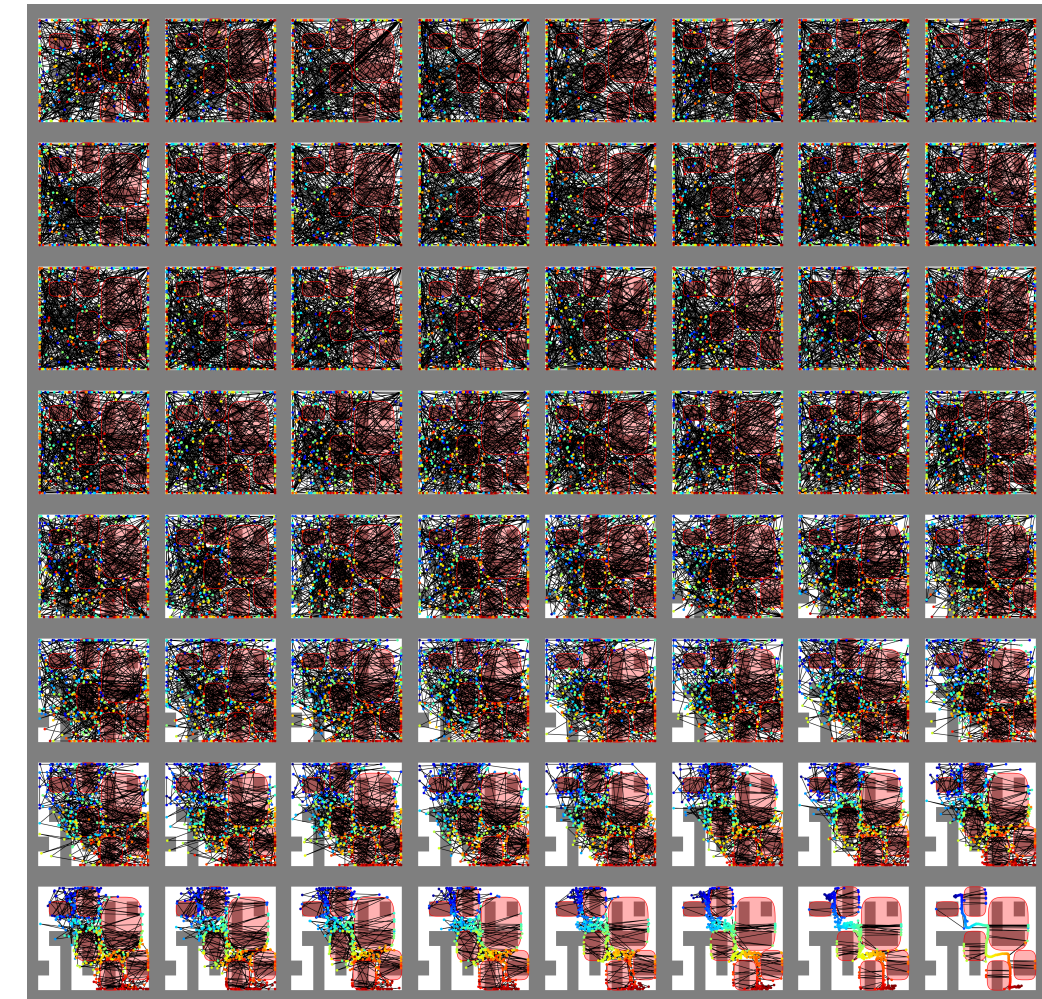


Figure 17: **Path Generation Process of SafeDiffuser (Xiao et al., 2025) in Maze2D environment with six constraints.** From the top-left to the bottom-right, we visualize τ_t on a uniform time discretization of $[T, 0]$, excluding the midpoint $t = 0.5T$.

1503

1504

1505

1506

1507

1508

1509

1510

1511

1512
 1513
 1514
 1515
 1516
 1517
 1518
 1519
 1520
 1521
 1522
 1523
 1524
 1525
 1526
 1527
 1528
 1529
 1530
 1531
 1532
 1533
 1534
 1535
 1536
 1537
 1538
 1539
 1540
 1541
 1542
 1543
 1544
 1545
 1546
 1547
 1548
 1549
 1550
 1551
 1552
 1553
 1554
 1555
 1556
 1557
 1558
 1559
 1560
 1561
 1562
 1563
 1564
 1565

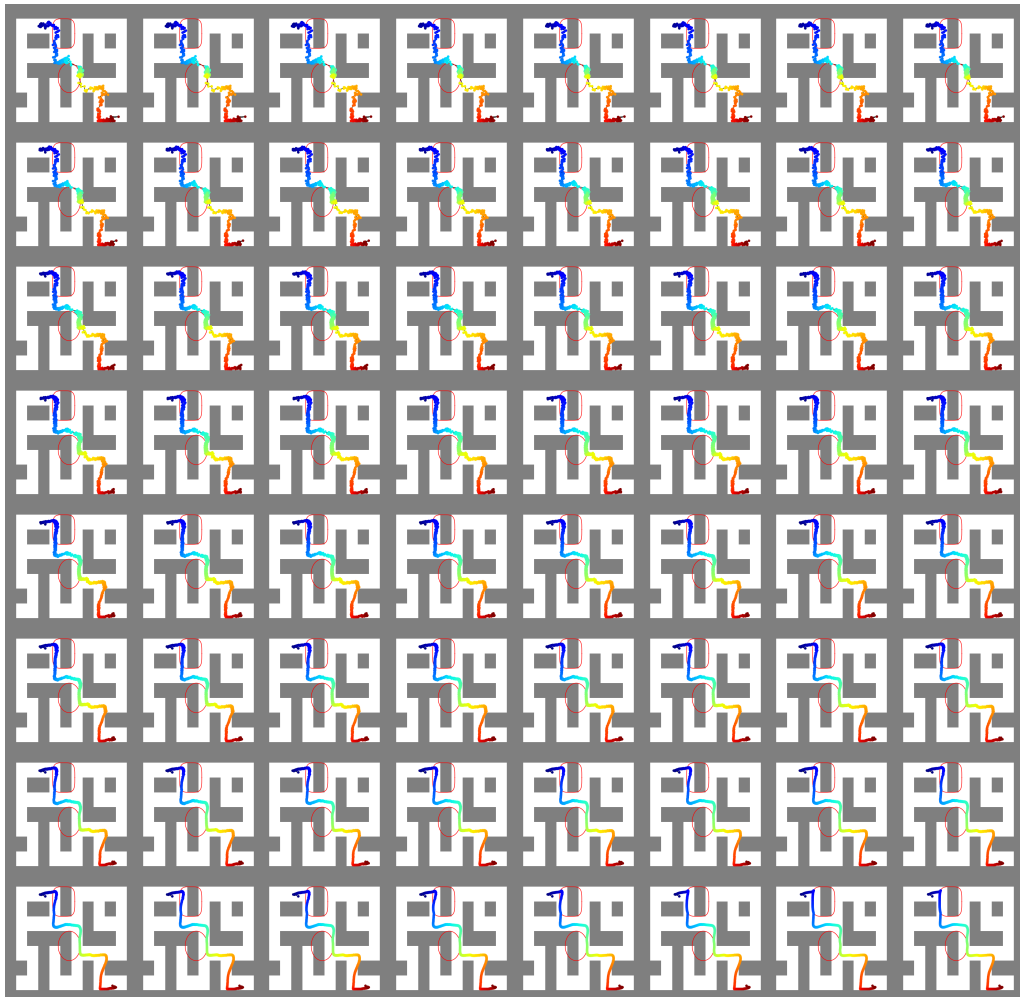


Figure 18: **Path Generation Process of SafeFlowMatcher in Maze2D environment with two constraints.** Top-left presents the predicted path $\tau_1^p = \tau_0^c$ from a noise sample. From the top-left to the bottom-right, we visualize τ_t^c on a uniform time discretization of $[0, 1]$, excluding the midpoint $t = 0.5$.

1566

1567

1568

1569

1570

1571

1572

1573

1574

1575

1576

1577

1578

1579

1580

1581

1582

1583

1584

1585

1586

1587

1588

1589

1590

1591

1592

1593

1594

1595

1596

1597

1598

1599

1600

1601

1602

1603

1604

1605

1606

1607

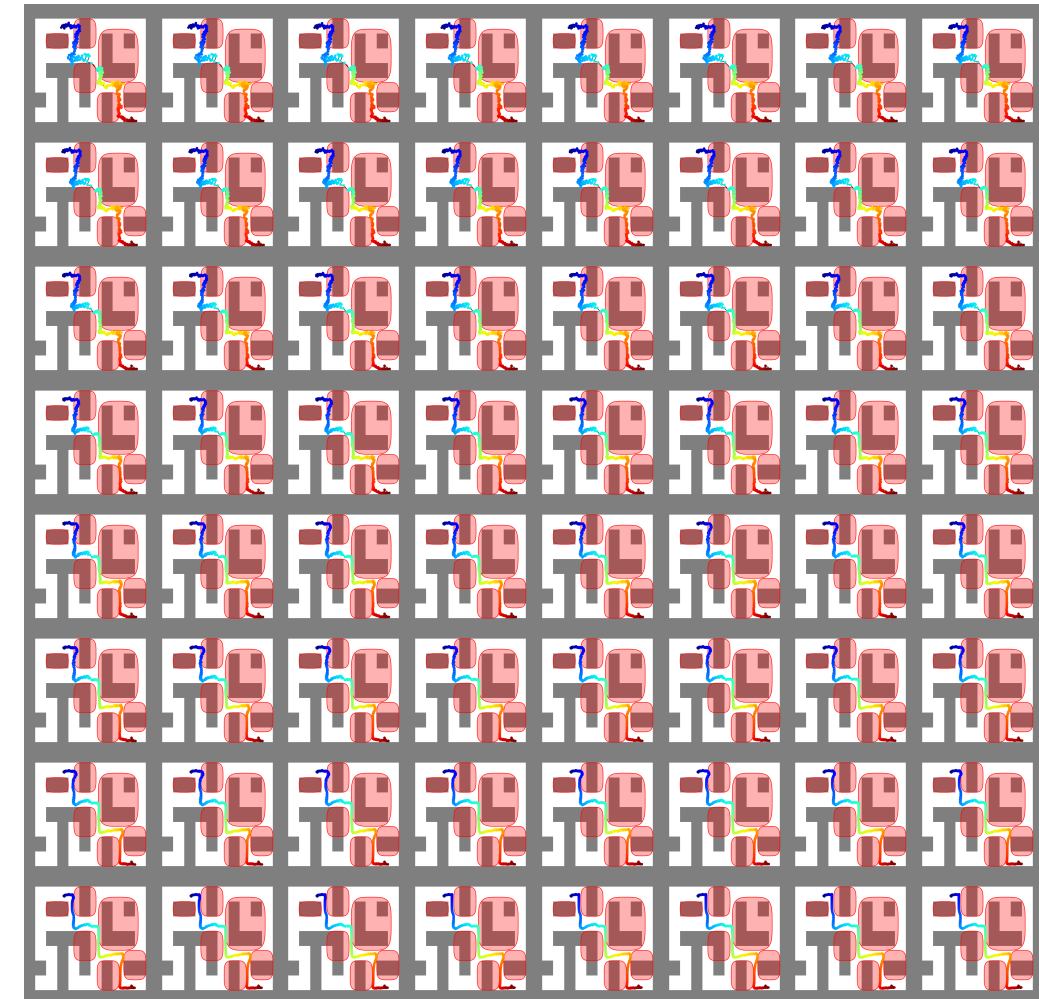


Figure 19: **Path Generation Process of SafeFlowMatcher in Maze2D environment with six constraints.** Top-left presents the predicted path $\tau_1^p = \tau_0^c$ from a noise sample. From the top-left to the bottom-right, we visualize τ_t^c on a uniform time discretization of $[0, 1]$, excluding the midpoint $t = 0.5$.

1611

1612

1613

1614

1615

1616

1617

1618

1619